



Influence of simple terrain on the spatial variability of a low-level jet and wind farm performance in the AWAKEN field campaign

William Radünz¹, Bruno Carmo¹, Julie K. Lundquist^{2,3}, Stefano Letizia², Aliza Abraham², Adam S. Wise^{4,5}, Miguel Sanchez Gomez², Nicholas Hamilton², Raj K. Rai⁶, and Pedro S. Peixoto⁷

¹Dynamics and Fluids Research Group, Escola Politécnica, University of São Paulo, São Paulo, SP, Brazil

²National Renewable Energy Laboratory, Boulder, CO, USA

³Johns Hopkins University, Baltimore, MD, USA

⁴University of California, Berkeley, CA, USA

⁵Lawrence Livermore National Laboratory, Livermore, CA, USA

⁶Pacific Northwest National Laboratory, Richland, WA, USA

⁷Institute of Mathematics and Statistics, Department of Applied Mathematics, University of São Paulo, São Paulo, Brazil

Correspondence: William Radünz (wradunz@usp.br)

Abstract. In wind energy research, scientific challenges are often associated with *complex terrain* sites, where orography, vegetation, and buildings disrupt flow uniformity. However, even sites characterized as *simple terrain* can exhibit significant spatial variability in wind speed, particularly during stable boundary layers (SBLs) and low-level jets (LLJs). This study investigates these terrain interactions using both simulations and observations from the American WAKE Experiment (AWAKEN). We employ a multiscale Weather Research and Forecasting (WRF) model simulation, integrating mesoscale forcing in the coarse domains and representing three rows of turbines from the King Plains wind farm as generalized actuator disks (GAD) in the large-eddy simulation (LES) domains. During a nocturnal LLJ event on 3 April 2023, the downwind, wake-affected turbine rows outperformed the upwind, unwaked row by 25–51 %. This counterintuitive result arises from terrain-induced streamwise variations in hub-height wind speed of approximately 4 m s^{-1} over 5 km—equivalent to $\sim 50 \%$ of the upwind reference speed. This enhancement outweighs the wake-induced reduction in mean wind speed ($\sim 12 \%$) and global blockage effects reported in the literature ($\sim 1\text{--}3.4 \%$). The multiscale simulations capture the intra-farm spatial variability in power performance observed in SCADA data. Terrain-induced vertical displacement of the LLJ, coupled with large wind shear below the jet maximum, drives the substantial streamwise acceleration within the wind farm. These findings underscore the importance of accounting for spatial variability related to terrain, even in simple landscapes, particularly during LLJ conditions. Incorporating such effects into reduced-order modeling frameworks for wind farm design and control could significantly enhance their effectiveness.

Copyright statement. This work was authored in part by the National Renewable Energy Laboratory, operated by Alliance for Sustainable Energy, LLC, for the U.S. Department of Energy (DOE) under contract no. DE-AC36-08GO28308. Funding was provided by the U.S. Department of Energy Office of Energy Efficiency and Renewable Energy Wind Energy Technologies Office. The views expressed in the article do not necessarily represent the views of the DOE or the U.S. Government. The U.S. Government retains and the publisher, by



22 accepting the article for publication, acknowledges that the U.S. Government retains a nonexclusive, paid-up, irrevocable, worldwide license to publish or reproduce the published form of this work, or allow others to do so, for U.S. Government purposes.

1 Introduction

24 One of the grand challenges in modern wind energy science is to measure, model and understand physical processes in
atmosphere–wind farm interactions that span a wide range of spatio-temporal scales (Veers et al., 2019, 2022). The soci-
26 etal motivation is to reduce the cost of energy, which can be achieved by at least two means. First, during the wind farm design
stage, an accurate understanding of the processes that modulate wind farm performance, backed up by observations and mod-
28 els, can help reduce uncertainty in the estimation of the annual energy production and design a wind farm that maximizes the
energy conversion. Second, for existing wind farms, appropriate observations and models that represent the relevant physical
30 processes are necessary for wind farm control. The existence of processes that create spatial gradients within the wind farm
area enhance the complexities associated with the design and optimization stages.

32 Spatial gradients in wind speed have paramount importance for the atmospheric sciences and wind energy. The vertical
gradient in wind speed is the wind shear and affects turbine performance (Sanchez Gomez and Lundquist, 2020; Murphy et al.,
34 2020) and loads (Sathe et al., 2013; Robertson et al., 2019; Lundquist, 2021). The wind results from interactions between
pressure gradient forces, Coriolis forces, and turbulent stresses. Horizontal gradients appear whenever a local imbalance in the
36 forces that drive the wind occurs, such as in the transition from surfaces of different roughness or heat flux (Stull, 1988), or for
flows over terrain with variable height (Baines, 1995). Horizontal gradients of velocity can be negligible compared to vertical
38 gradients over isothermal flat terrain with uniform roughness and thermal properties in the microscale range. Indeed, landmark
field campaigns were held in sites with flat and homogeneously covered terrain (Kaimal and Wyngaard, 1990; Holtslag et al.,
40 2012) to minimize such spatial variability.

During the nighttime over land, surface cooling produces thermal stratification that inhibits turbulent motions in the planetary
42 boundary layer, resulting in a stable boundary layer (SBL). A myriad of processes can occur in SBLs, such as atmospheric
gravity waves, topographic acceleration or blocking of winds, turbulence intermittency, and low-level jets (LLJs) (Poulos et al.,
44 2002; Fernando et al., 2019). A LLJ is a stream of fast-moving air with a maximum in wind speed relatively close to the ground,
which is enabled by the suppression of frictional forces in the upper portion of the SBL. Distinct physical mechanisms can form
46 LLJs (Blackadar, 1957; Holton, 1967; Stensrud, 1996; Banta et al., 2002; Banta, 2008; Klein et al., 2015; Smith et al., 2019a),
and once formed, it can manifest at least three turbulence regimes (Banta, 2008): a weakly-stable regime with continuous
48 turbulence, a very-stable regime with almost no turbulence, and a transitional or intermittent regime with occasional bursts of
turbulence. In the Southern Great Plains (SGP) of the United States, LLJs display these different turbulence regimes (Klein
50 et al., 2015) and accompanying large spatio-temporal variability in their evolution (Banta et al., 2002; Smith et al., 2019a).

There is an important link between terrain complexity, SBLs and LLJs in the modulation of the spatial variability of the
52 wind. The existence of horizontal variability introduces an additional complexity, because one can no longer assume a single
wind profile is representative of the entire site. In stable conditions, the low-level wind decelerates upstream of obstacles more



54 than it would in neutral conditions because of the downward buoyancy (Mahrt and Larsen, 1990; Baines, 1995; Hunt et al.,
1988) forcing the flow to stay at the same altitude rather than rising over the obstacles. Likewise, the flow accelerates more in
56 the lee, and this combination enhances the spatial variability in wind speed. This behavior happens, to a lesser or higher degree,
to any SBL, from which the LLJs are a particular case. This variability is one of the main scientific challenges associated with
58 complex terrain, and motivated for example a large-scale field campaign and model development effort in the New European
Wind Atlas (NEWA) project (Mann et al., 2017). The Perdigão (Fernando et al., 2019) and the Alaiz (Santos et al., 2020)
60 experiments from the NEWA revealed with unprecedented detail the variability in flow patterns that occurred when stable
boundary layers (SBLs) and nocturnal low-level jets (LLJs) interacted with complex terrains (Peña and Santos, 2021; Wagner
62 et al., 2019; Wise et al., 2022). In (Banta et al., 2002), sometimes the LLJ observations suggested the flow followed the terrain,
whereas sometimes it remained at a constant height above mean sea level (AMSL). Other investigations also pointed out to the
64 terrain-induced variability in wind speed in stable conditions (Mahrt et al., 2021; Radünz et al., 2020).

The terrain-induced variability in wind speed during SBLs and LLJs can lead to important spatial variations in power
66 performance over complex terrain (Radünz et al., 2021, 2022). Other physical processes that can modulate farm performance
in SBLs include wind farm wakes (Doosttalab et al., 2020; Gadde and Stevens, 2021) and blockage (Wu and Porté-Agel, 2017;
68 Bleeg et al., 2018; Sebastiani et al., 2021; Schneemann et al., 2021; Sanchez Gomez et al., 2022). In Radünz et al. (2021), wind
farms built in complex terrain were investigated because the back rows produced at times twice as much power as the front
70 rows, despite the downwind wake effects undermining performance in the back rows. This performance pattern was associated
with a strong downwind flow acceleration in stable conditions. The back rows were closer to the lee of the plateau, and thus
72 had stronger winds available in comparison with the front rows. Later on, the occurrence of nocturnal jets and the depth of the
stable layer were shown to amplify the horizontal variability in the winds and turbine performance (Radünz et al., 2022).

74 Specific attributes of the LLJ may make it particularly susceptible to terrain-induced accelerations, even in the presence of
simple topographic features, potentially causing substantial changes in wind speed and wind farm performance. However, most
76 existing research on LLJ interactions with wind farms has relied on idealized numerical simulations, leaving a critical gap in
the understanding of real-world interactions involving LLJs, terrain, and operational wind farms. This gap underscores the need
78 for field measurements and operational data to validate and improve models. The American WAKE ExperimeNt (AWAKEN),
an international wind energy science project funded by the United States Department of Energy (DOE) and led by the National
80 Renewable Energy Laboratory (NREL), aims to address this gap by advancing the physical understanding and modeling of
atmosphere–wind farm interactions (Debnath et al., 2022; Moriarty et al., 2024). The study site, located in the U.S. Southern
82 Great Plains (SGP) of northern Oklahoma, was chosen due to its dense concentration of wind farms, the availability of high-
quality historical observations from the Atmospheric Radiation Measurement (ARM) Program’s SGP facility (Krishnamurthy
84 et al., 2021a), and the frequent occurrence of meteorological phenomena of interest for wind energy, such as southerly LLJs
(Banta et al., 2002; Banta, 2008; Klein et al., 2015; Smith et al., 2019a; Krishnamurthy et al., 2021b). This field campaign
86 provides an excellent setting for evaluating the two key goals of our investigation: (1) assessing whether simple terrain can
induce significant spatial variability in wind speed, thereby influencing turbine wakes and performance, and (2) determining
88 whether specific LLJ characteristics amplify terrain-induced spatial wind variability.



This paper investigates the interaction between a southerly nocturnal LLJ on 3 April 2023 and a seventeen-turbine subset
90 of the King Plains wind farm, the most heavily instrumented site in the AWAKEN project. The terrain at the site is neither
traditionally complex (e.g., mountainous or hilly) nor entirely flat, consisting of shallow river valleys with elevation changes
92 of less than 50 m—referred to here as simple terrain. The remainder of the paper is organized as follows. Section 2 describes
the orography and land use characteristics of the AWAKEN site, the observational dataset, criteria for case selection, and the
94 simulation setup. The simulations use a multiscale WRF-LES-GAD (generalized actuator disk) approach, realistically driven
by High-Resolution Rapid Refresh (HRRR) v4 analysis data. Section 3 integrates observations from ground-based scanning
96 and profiling lidars, an atmospheric emitted radiance interferometer, and a sonic anemometer to validate the simulations and
analyze the planetary boundary layer (PBL) winds, stability, and turbulence across the wind farm. Turbine performance is
98 assessed using supervisory control and data acquisition (SCADA) system data. Section 4 provides a conceptual description of
terrain-induced wind variability and compares its significance with wake and blockage effects. It also discusses the implications
100 of terrain effects for multiscale modeling and wind farm control, as well as the potential long-term manifestation of terrain-
induced variability associated with LLJs. Finally, Section 5 presents the main conclusions and outlines directions for future
102 research.

2 Methods

104 2.1 The AWAKEN field campaign observations and case study selection

Five wind farms were selected for the AWAKEN field campaign, which are King Plains, Armadillo Flats, Breckenridge,
106 Chisholm View, and Thunder Ranch (Fig. 1). This investigation focuses on the eastern portion of the King Plains wind farm
because it is the most well instrumented location in AWAKEN. Furthermore, in the prevailing southerly winds (Debnath et al.,
108 2022; Moriarty et al., 2024), it is not directly downwind of other wind farms. Therefore, the power performance patterns in
eastern King Plains are solely caused by the terrain effects and turbine interactions that belong to that wind farm. We focus on
110 a subset of 17 turbines organized into three rows.

The observations from the field campaign enable testing several scientific hypotheses, four of which are related to our work:
112 the (i) wind farm wakes propagation (Bodini et al., 2024; Cheung et al., 2023; Krishnamurthy et al., 2024), (ii) blockage (Che-
ung et al., 2023; Sanchez Gomez et al., 2022), (iii) wake steering and (iv) individual turbine wake morphology. The AWAKEN
114 site has relatively simple terrain, such that even the names of the wind farms bring this feature: *King Plains*, *Armadillo Flats*.
Thus, understanding the terrain-induced spatial variability and influence of LLJs is relevant to the aforementioned scopes.

116 Observations from the A1 and A2 sites characterize the inflow because they contain no interference from nearby wind farms
(Fig. 2) and are used for the case selection and model validation. At site A1, immediately upwind of the King Plains wind
118 farm in the southerly wind direction, wind speed components were measured with a Halo scanning lidar (Letizia and Bodini,
2023). Reynolds stresses from this lidar were estimated based on the six-beam method of Sathe et al. (2015). Also at site A1,
120 a Windcube v. 2 profiling lidar measured the wind speed components with a sampling rate between 0.5 to 1 s between 40 and
240 m above ground level (AGL) with a vertical resolution of 20 m (Wharton, 2023). A sonic anemometer at an upwind site

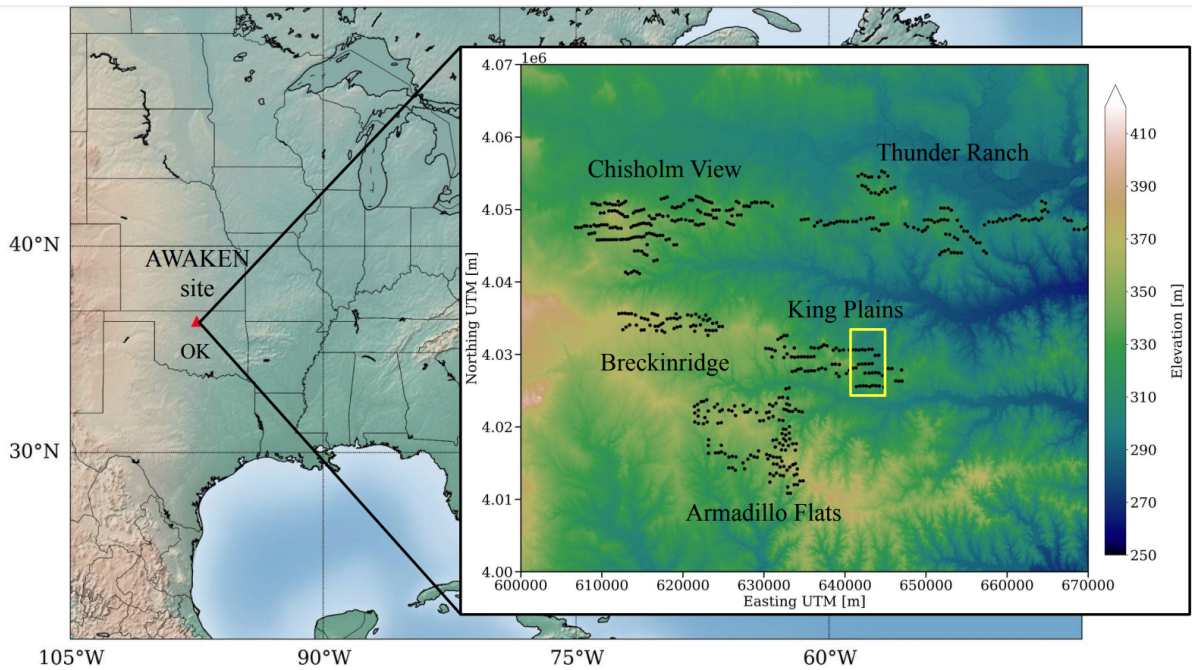


Figure 1. The background map of the United States of America (USA) shows the location of the AWAKEN site in Oklahoma (OK) near [36.5 °N, -97.5 °W]. In the foreground, the five wind farms that integrate the AWAKEN field campaign are shown overlaid on the terrain elevation map: King Plains, Armadillo Flats, Breckinridge, Chisholm View, and Thunder Ranch. The eastern portion of the King Plains wind farm is the focus of our investigation (yellow rectangle).

122 A2 measured wind speed components at a sampling rate of 20 Hz at 4 m AGL (Pekour, 2023). Although a profiling lidar was
also located at A2, its poor data quality from 04:00 to 06:00 UTC during this case study was insufficient for analysis. Potential
124 temperature profiles at site C1 (Atmospheric Radiation Measurement Southern Great Plains Central Facility) were derived
from ground-based atmospheric emitted radiance interferometer (AERI) observations (Shippert and Zhang, 2016) using the
126 TROPoe retrieval algorithm (Turner and Löhnert, 2014; Turner and Blumberg, 2019).

The case study consists of a southerly LLJ during a somewhat stationary window to mitigate the influence of larger-scale
128 dynamic events in the analysis. Also, we selected nights with sufficiently strong winds to create turbulent motions resolvable
with a $dx = 5$ m grid (Skamarock, 2004), but not as strong as to cause turbines to operate near rated capacity, and thus impair
130 our capacity to assess spatial variability in performance. Nights with weak winds create relatively small-scale turbulent motions
that require a fine computational grid to be resolved. We also wanted stationary and moderate values for the sensible heat flux
132 to avoid changes in the surface forcing. There were no requirements for the spatial variability in winds and performance. The
case selection considered the following requirements. During the nighttime between 04:00 and 12:00 UTC, the time-averaged
134 (i) wind speed at 100 m AGL should be between 5 and 14 m s⁻¹, (ii) wind direction at 100 m AGL between 160° and 200°,

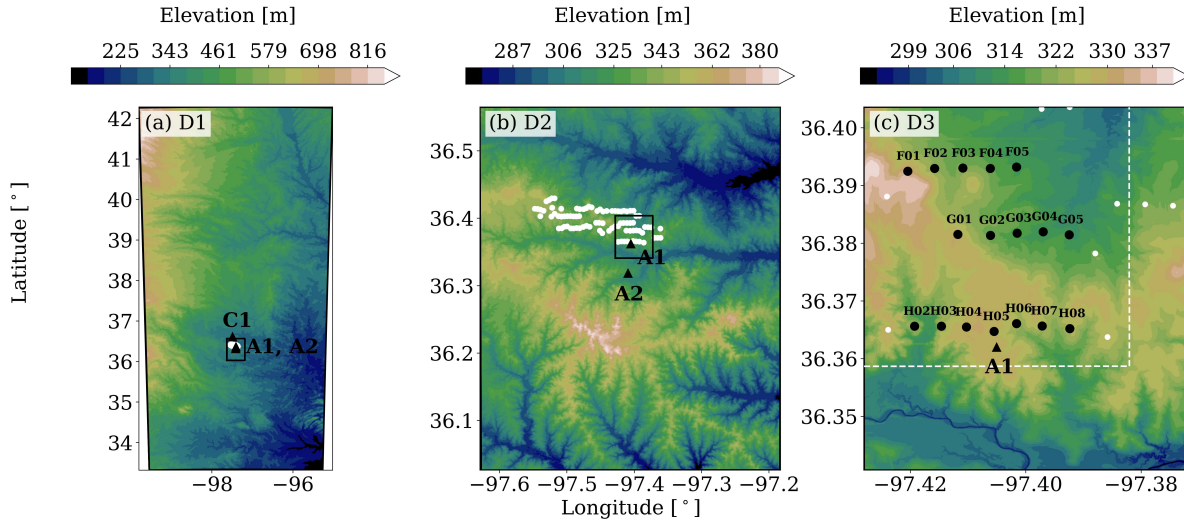


Figure 2. Horizontal extent and terrain elevation maps associated with the WRF simulations domains D1 (a), D2 (b) and D3 (c). The King Plains wind farm consists of 88 turbines (white dots), from which a subset of 17 wind turbines was represented in the simulation (black dots). Within domain D3, some turbines near boundaries were removed (white dots). Inflow fetches of 2 and 1 km in the southerly and easterly boundaries, respectively, were removed from the analyses (white dashed lines). The observation sites A1, A2 and C1 (black triangles) are also shown.

(iii) the standard deviation in wind direction at 100 m AGL below 50° , (iv) the sensible heat flux lower than -20 W m^{-2} and
 136 the (v) friction velocity lower than 0.5 m s^{-1} .

The dates from the year of 2023 that meet these criteria are 3 April, 18 April and 15 May 2023. Ultimately, 3 April 2023
 138 was selected because of the predominant southerly wind direction (180°) and the moderate winds with large sensible heat flux,
 suggesting vigorous nighttime turbulence. The selected analysis window was from 04:50 to 05:25 UTC because of curtailment
 140 events at other times and occurrence of clouds in the simulations later on at 08:00 UTC.

2.2 Simulation setup

142 The multi-scale simulations were performed with the Advanced-Research Weather Research and Forecasting (WRF) model
 version 4.1.5 (Skamarock et al., 2019), which solves the compressible Euler equations for the three spatial dimensions and
 144 time. Three computational domains with a progressive increase in spatial resolutions and smaller areas were used to represent
 and bridge the large-scale, mesoscale, and microscale atmospheric processes (Fig. 2). The grid details specific to each domain
 146 are described in Table 1. For instance, the outermost domain (D1) had 201, 501 and 101 cells in the x (west to east), y (south
 to north) and z (vertical) directions with a fixed horizontal resolution of $\Delta x = \Delta y = 2000 \text{ m}$. In the vertical direction, the grid
 148 consisted of a finer and near-constant layer of $\Delta z_{sfc} = 30 \text{ m}$ in the first 1 km AGL, which was stretched out to a maximum of
 $\Delta z = 300 \text{ m}$ at the domain top. The large jump in spatial resolution between domains D1 ($\Delta x = 2000 \text{ m}$) and D2 ($\Delta x = 100 \text{ m}$)



Table 1. Computational grid and temporal information by domain.

Parameter	D1	D2	D3
$\Delta x, \Delta y$ [m]	2000	100	5
Δz_{sfc} [m]	30	20	4
n_x	201	401	1001
n_y	501	601	1401
n_z	101	121	168
Start time	2 April 2023 12:00 UTC	3 April 2023 03:00 UTC	3 April 2023 04:30 UTC
End time	3 April 2023 05:25 UTC	3 April 2023 05:25 UTC	3 April 2023 05:25 UTC
Time step [s]	12	0.6	0.025

150 was intended to skip over the *terra incognita* (Wyngaard, 2004), where turbulence length scales are of the same order as the
 horizontal grid spacing ($100 < \Delta x < 1000$ m) (Muñoz-Esparza et al., 2017; Rai et al., 2019), as in the multiscale simulations
 152 of Muñoz-Esparza et al. (2017). The innermost nest domain (D3) had a fixed horizontal resolution of $\Delta x = 5$ m. Each domain
 used a different vertical grid (vertical nesting (Daniels et al., 2016)), and the innermost domains were finer, such as done in
 154 other multiscale simulations (Wise et al., 2022; Sanchez Gomez et al., 2022; Wagner et al., 2019).

The static datasets employed for the terrain elevation and land use categories were the United States Geological Survey
 156 (USGS) 1/3 arc-second ($\Delta x \approx 10$ m) dataset (U.S. Geological Survey., 2020) and the National Land Cover Dataset 2019
 1 arc-second ($\Delta x \approx 30$ m) dataset (U.S. Geological Survey., 2019), respectively. The coarser Global Multi-resolution Terrain
 158 Elevation Data 2010 (Danielson and Gesch, 2011) with a resolution of 30 arc-second ($\Delta x \approx 1000$ m) was used for domain D1.

The terrain features can be described in terms of various scales. The domain D1 covers the foothills east of the Rocky
 160 Mountains to the west and the sloping terrain that includes the SGP in the center and eastern regions (Fig. 2a). The domain D2
 demonstrates that the terrain near the AWAKEN site is characterized by small river valleys and ridge lines with a domain-wise
 162 maximum variation in elevation (amplitude) of 118 m (Fig. 2b). The innermost domain D3 displays the microscale terrain
 features in the King Plains wind farm area, with a domain-wise elevation amplitude of 49 m (Fig. 2c). The succession of the
 164 small river valley depression near the southern boundary, the smooth ridge line and the beginning of the down-slope area that
 leads to the larger river valley further north appear at higher resolution. A subset of 17 turbines is represented in the finest
 166 domain of the simulations. The turbines in the first row (H02–H08) are sited over slightly higher ground ($z \sim 330$ m AMSL),
 and those in the second (G01–G05) and third (F01–F05) rows are sited in the small down-slope area ($z \sim 320$ m AMSL),
 168 which is shown in detail in the Appendix (Fig.A1c). Because of microscale terrain features, turbines H02, H03 and H06–H08
 are located at local lower ground, and turbine F01 is at higher ground.

170 The initial and boundary conditions were provided by the High-Resolution Rapid Refresh (HRRR) model v4 (Dowell et al.,
 2022; National Oceanic and Atmospheric Administration (NOAA), 2024), with a horizontal spatial and temporal resolutions
 172 of 3 km and 1 h, respectively. In this case study, simulations forced by the European Centre for Medium-Range Weather
 Forecasts Reanalysis v5 (ERA5) (Hersbach et al., 2020) and the North American Mesoscale Forecast System (NAM) (Rogers
 174 et al., 2009) models data sets produced an exaggerated stratification and a weaker LLJ (Radünz et al., 2023), although other



176 studies of LLJ in this region (Smith et al., 2019a, b) have found success with NAM. The WRF simulation was from 2 April
2023 12:00 UTC to 3 April 2023 05:25 UTC, allowing 12 hours of spin-up time before the evening transition period at 00:00
UTC (Table 1). The domains were activated sequentially during the spin-up time. Considering an estimated 20-minute spin-up
178 time for the D3 domain, the analysis period was between 3 April 2023 04:50 and 05:25 UTC (35 min).

Several processes were included via parameterization schemes, such as for cloud microphysics, radiation, and the exchange
180 of momentum, heat, and moisture with the land surface. The main physics options adopted for each domain are summarized in
Table 2. All domains used the WRF Single-Moment 3-class simple ice scheme (Hong et al., 2004) for cloud microphysics, the
182 RRTM (Mlawer et al., 1997) scheme for short- and longwave radiation processes, and the Noah land surface model (Chen and
Dudhia, 2001). No cumulus parameterization option was included in any domain due to the fine resolution.

Table 2. Physics parameterization by domain. The model references are found in the text.

Physics	D1	D2	D3
Cumulus	–	–	–
Microphysics	WSM3	WSM3	WSM3
Longwave radiation	RRTM	RRTM	RRTM
Shortwave radiation	RRTM	RRTM	RRTM
Land surface	Noah	Noah	Noah
Surface layer	MYJ	MYJ	MYJ
Planetary boundary layer	MYJ	–	–
LES SGS	–	1.5TKE	NBA2
CPM	–	–	on
GAD	–	–	on

184 Turbulent processes in the planetary boundary layer (PBL) were accounted for differently in mesoscale and microscale
domains. In the outermost domain D1, turbulence was modeled using the Mellor–Yamada–Janjic (MYJ) PBL parameterization
186 scheme (Janjić, 1990; Janić, 2001), such as in other LLJ studies in the SGP (Storm et al., 2009; Storm and Basu, 2010;
Vanderwende et al., 2015). The Mellor–Yamada–Janjic (MYJ) surface-layer (SL) scheme was employed for all domains. In
188 the nested domains (D2 and D3), LES resolves turbulent motions larger than the grid size, and the influence of the interaction
between subgrid and resolved-grid motions on the resolved-grid flow field were modeled via subgrid-scale (SGS) models. As
190 in Zhou and Chow (2014) and Wise et al. (2024), different SGS models were used for the coarse and the fine LES domains.
The Deardorff 1.5 TKE SGS model (Deardorff, 1980) was used for domain D2. The nonlinear backscatter and anisotropy
192 (NBA) SGS model (Kosović, 1997), which accounts for backscatter and can improve turbulence dynamics, was used for the
innermost domain D3. SGS models that include backscatter are useful in multiscale simulations of stratified flows (Zhou and
194 Chow, 2014; Sanchez Gomez et al., 2022; Wise et al., 2024).

To accelerate the spin-up of turbulence within the innermost domain, we applied the cell perturbation method (CPM)
196 (Muñoz-Esparza et al., 2014, 2015; Muñoz-Esparza and Kosovic, 2018) in the southern and eastern boundaries. The CPM
applies random perturbations to the potential temperature field to trigger buoyancy fluctuations and shorten the fetch required



198 for turbulence spin-up. The current implementation in WRF dynamically uses information from the diagnosed PBL height
 from the mesoscale domain to confine perturbations vertically. The potential temperature perturbation amplitude was calcu-
 200 lated based on Muñoz-Esparza and Kosovic (2018) for a turbulent Eckert number (E_c) of 0.2. The CPM was deactivated for
 domain D2 because it was too coarse to resolve turbulence in stable conditions, the same rationale used in (Wagner et al.,
 202 2019). The turbulence was sufficiently spun-up between 1.5 and 2 km from the southerly boundary of domain D3 (Fig. B1 in
 the Appendix). Thus, the analysis considers as a fully spun-up region a domain subset of 4 by 5 km, where 2 km and 1 km are
 204 removed from the southerly and easterly boundaries of domain D3, respectively (Fig. 2c).

Wind turbines were represented in the simulations as generalized actuator disks (GAD) (Mirocha et al., 2014; Aitken et al.,
 206 2014; Arthur et al., 2020). The GAD computes the axial and tangential forces imparted by the turbine to the flow based on
 the aerodynamic properties of the blade and turbine control strategy. To circumvent the need for proprietary data, the GE 2.8-
 208 127 turbine model installed in King Plains was emulated using an OpenFAST model. Publicly available turbines were used
 as a template, and characteristics were tuned to match the GE 2.8-127 power and thrust curves (Quon, 2022). In addition to
 210 the simulation with the wind turbines, a second simulation with the same configuration but without the wind turbines was
 performed. This procedure enabled isolating the turbine wake effects.

212 3 Results

3.1 Wind, stability and turbulence in the planetary boundary layer

214 To assess the simulation skill in representing relevant rotor layer and surface quantities, a time series of selected variables
 is compared against observations from a profiling lidar at site A1 and a nearby sonic anemometer at site A2 at 4 m AGL
 216 (Fig. 3). A 10 minute rolling window is used to compute the instantaneous turbulence-related variables sensible heat flux (H_s)
 and vertical velocity variance ($\overline{w'w'}$). The gray shaded area in Fig. 3 marks the 20 minute spin-up time, and the analysis is
 218 conducted during the period between 04:50 and 05:25 UTC. The time averaged summary of the inflow conditions are shown in
 Table 3. The subscripts in the variables denote the height AGL. The variables are the wind speed (WS_{90} and direction (WD_{90}
 220 at 90 m AGL, wind shear exponent between 40 and 160 m AGL (α_{40-160}), wind veer between 40 and 160 m AGL expressed in
 degree every 100 m (β_{40-160}), sensible heat flux at the surface (H_s) and vertical wind velocity variance at 90 m AGL ($\overline{w'w'_{90}}$).

Table 3. Time averaged values associated with the wind inflow of the 3 April 2023 case study between 04:50 and 05:25 UTC.

Source	WS_{90} [m s^{-1}]	WD_{90} [$^\circ$]	α_{40-160} [-]	β_{40-160} [$^\circ 100 \text{ m}^{-1}$]	H_s [W m^{-2}]	$\overline{w'w'_{90}}$ [$\text{m}^2 \text{ s}^{-2}$]
WRF-A1 (D3)	8.22	167	0.094	4.4	-43	0.23
OBS-PL-A1	8.09	167	0.170	7.5	-	0.21
OBS-SNC-A2	-	-	-	-	-57	-

222 The wind speed ($\approx 8.22 \text{ m s}^{-1}$) and direction ($\approx 167^\circ$) remain in the range between $5\text{--}10 \text{ m s}^{-1}$ and $160\text{--}175^\circ$ (southerly
 winds), respectively, matching well the observations (Fig. 3a and b). Again, the reader may refer to Table 3 to verify the
 224 average values. The wind shear exponent (Fig. 3c, calculated between 40 m and 160 m) is underestimated in the simulations

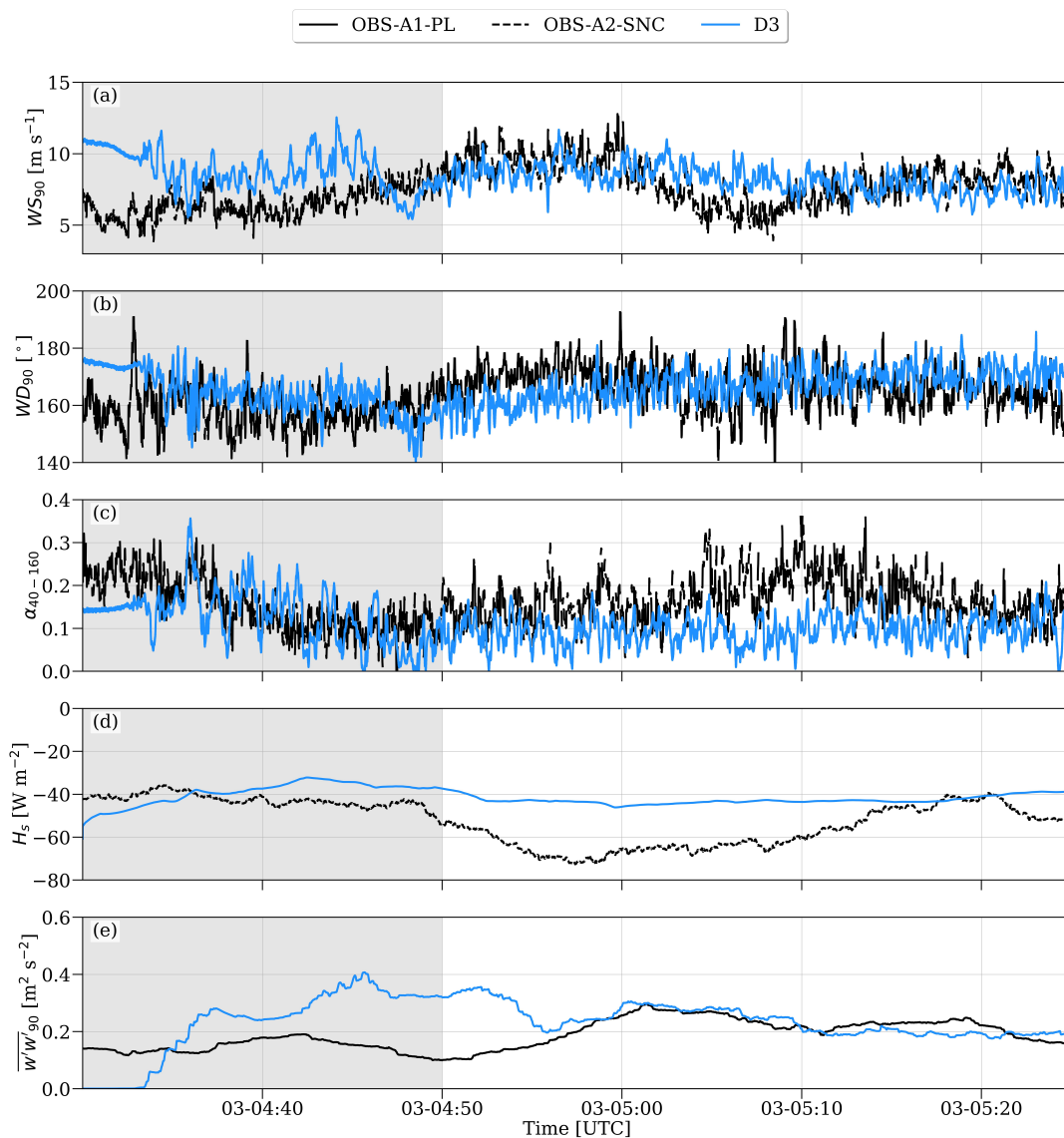


Figure 3. Time series of wind speed (WS_{90} , a) and direction (WD_{90} , b) at 90 m AGL, wind shear exponent between 40 and 160 m AGL (α_{40-160} , c), sensible heat flux at the surface (H_s , d) and vertical wind velocity variance at 90 m AGL ($\overline{w'w'}_{90}$, e). The subscripts in the variables denote the height AGL. A 10-minute rolling window is used to compute H_s and $\overline{w'w'}$. Observations from the profiling lidar at site A1 (OBS-A1-PL) and the sonic anemometer at site A2 (OBS-A2-SNC) are represented as continuous and dashed black lines, respectively. Simulation results for domain D3 are represented as continuous blue lines. The gray shaded area marks the 20 minute spin-up time.



(~ 0.094) relative to the observations (~ 0.170). Observed wind speed (shear) decreases (increased) between 05:00 and 05:20
226 UTC, which does not occur in the simulations. Noticeably, the temporal fluctuations in the wind speed and direction signals
are similar in amplitude and frequency to the observed ones. As in Muñoz-Esparza et al. (2017), this behavior indicates that
228 the turbulent motions were consistently resolved in the simulations.

Simulated turbulence metrics are within the range of values observed. The turbulence-related metrics, sensible heat flux at
230 the surface (Fig. 3d) and vertical velocity variance at 90 m AGL (Fig. 3e), approach the observed values. The simulated heat
flux time series is, on average, (-43 W m^{-2}), weaker than observed values (-57 W m^{-2}). The simulated vertical velocity
232 variance ($0.23 \text{ m}^2 \text{ s}^{-2}$) is, on average, close to the observed values ($0.21 \text{ m}^2 \text{ s}^{-2}$).

The vertical structure of the boundary layer associated with the LLJ computed in the simulations matches well the observed
234 time-averaged wind speed, direction and potential temperature profiles, with a few differences (Fig. 4a–c). The observed LLJ
speed profile has a maximum of about 24 m s^{-1} at roughly 500 m AGL with an almost linear increase with height from the
236 surface to the nose (Fig. 4a), such as described in Banta (2008). The simulation results displays a somewhat flatter nose, below
which the wind shear is stronger than in the observations ($300 < z < 400 \text{ m AGL}$). Between 26.5 and 300 m AGL, the wind
238 shear is slightly weaker than in the observations. The potential temperature profile is stably stratified as in the observations,
but the stratification is weaker between 26.5 and 300 m AGL in the simulations (Fig. 4c). Conversely, the stratification in
240 the simulation is higher than in the observations between 300 and 400 m AGL. However, the interpretation of the observed
potential temperature profile should be used with caution: AERI retrievals are affected by poorer vertical resolution away from
242 the ground compared to the LES (Turner and Löhnert, 2014), which could explain some differences with the simulations.
Also, the potential temperature profile at the C1 site is merely a proxy for the stratification at the A1 site, since there are
244 no measurements of this type there. The magnitude and vertical variation with height of the wind direction (veer) is well
represented. The wind direction veers considerably with height, by about 4.4° every 100 m near the rotor (40 to 160 m AGL).
246 Scanning and profiling lidar observations are consistent, although the profiling lidar displays more variability, likely due to the
smaller measurement volume and shorter temporal averaging period (Robey and Lundquist, 2022).

248 The turbulence-related variables calculated are consistent with observations (Fig. 4d,e) and the expected behavior for strong
LLJs (Banta, 2008; Klein et al., 2015) as the strong wind shear results in mechanically-generated turbulence. The turbulence
250 intensity (TI) was computed as the ratio between the standard deviation and the mean of the 10-minute wind speed. The $\overline{w'w'}$
profile displays strong turbulence above rotor bottom tip ($z < 26.5 \text{ m AGL}$) and below 300 m AGL, with a maximum near
252 the rotor top tip ($z < 153.5 \text{ m AGL}$). This enhanced mixing weakens the stratification in the aforementioned layer. Below
 $z = 26.5 \text{ m}$, the simulated $\overline{w'w'}$ is small and reaches zero at the surface. The associated peak in TI near the surface was caused
254 by the very small wind speed. Thus, near the surface, the stratification increased. These features are consistent with a strong
LLJ, whereby turbulence is continuously produced below the jet nose owing to mechanical shear (Banta, 2008; Klein et al.,
256 2015). Because shear is small near the jet nose, so is turbulence, as mean shear is the main driver of mechanical production of
turbulent kinetic energy.

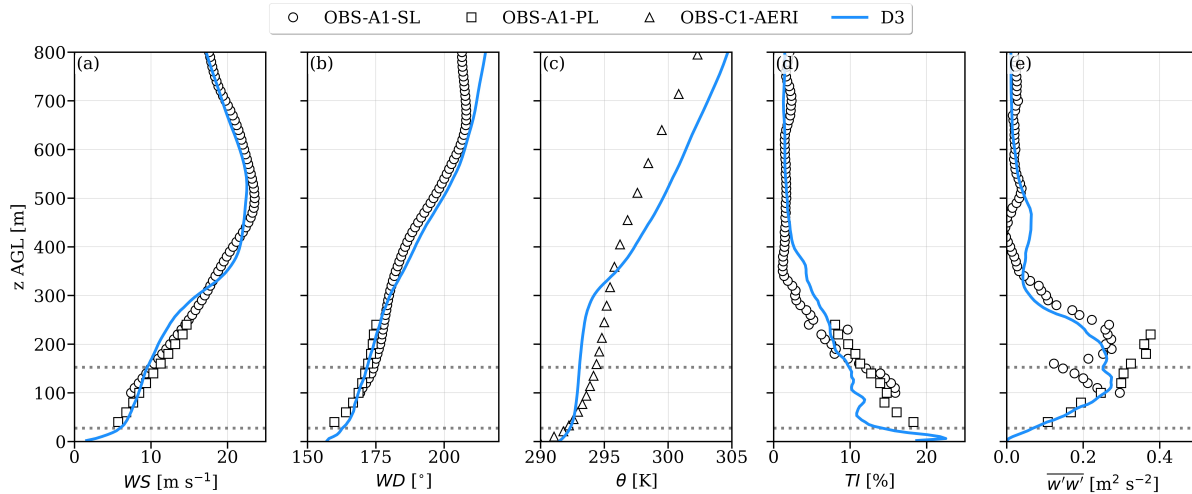


Figure 4. Vertical profiles of wind speed (a), direction (b), potential temperature (c), TI (d) and $\overline{w'w'}$ (e) for a 30 minute window between 04:55 and 05:25 UTC. Observations from the scanning lidar at site A1 (OBS-A1-SL), the profiling lidar at site A1 (OBS-A1-PL), and the AERI at site C1 (OBS-C1-AERI) are represented as markers. Results from domain D3 are represented as blue continuous lines.

258 Both the mean flow and the turbulence-related variables reasonably approximate the observations in the rotor layer and
above. Therefore, the simulated flow field elsewhere is likely to approximate the behavior of the real flow field. Hence, we now
260 examine the wind farm performance patterns and their relation to the flow field.

3.2 Wind farm performance

262 This section evaluates the power performance variability within the wind farm. The turbine power acquired with the supervisory
control and data acquisition (SCADA) system is normalized as requested by the wind farm owner in the Non-Disclosure
264 Agreement (NDA). The normalized mean power is computed as the ratio between the mean power of each row and the turbine
rated power ($= P_{row}/P_{rated}$). The normalized mean power is separated into first (turbines H02–H08), second (turbines G01–
266 G05) and third (turbines F01–F05) rows. For the southerly wind direction, the first row is upwind of the second and third
rows.

268 An unexpected performance pattern occurs in the normalized mean power time series because the second and third rows
consistently outperform the front row (Fig. 5) throughout this time period, even though the second and third rows should
270 be impacted by wakes from the first row. This overperformance for the downwind rows occurs in both the observations and
simulations. Further, the normalized mean power of the third row (SCADA = 0.937, WRF = 0.939) is slightly larger than that
272 of the second row (SCADA = 0.776, WRF = 0.894). Both the mean power of the third and second rows are larger than that
of the first row (SCADA = 0.621, WRF = 0.629). In percent, the first row is outperformed by the third (SCADA = 51 %,
274 WRF = 51 %) and second (SCADA = 25 %, WRF = 44 %) rows. Although the simulated power of the second row is higher
than that derived from the SCADA, the agreement for the first and third rows is better.

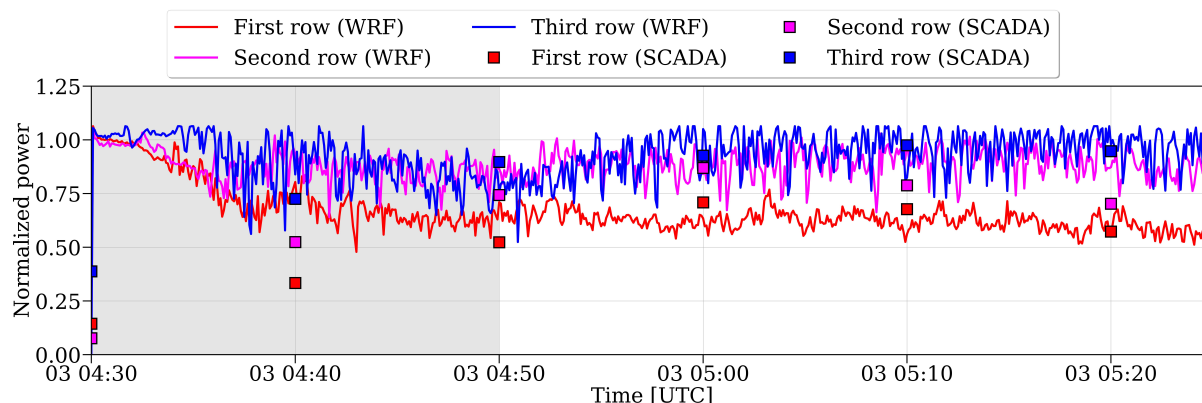


Figure 5. Time series of normalized mean power based on simulations (continuous lines) and SCADA data (markers). The gray shaded area marks the 20 minute spin-up time.

276 This performance differential was unexpected because the first row is free of wakes for the southerly wind direction and the
278 second and third rows are likely to experience wake effects. Additionally, because of the gentle or simple terrain, the spatial
280 variability of winds was expected to be small. Given these circumstances, the first row was expected to outperform the back
rows. Thus, some physical processes must have induced large spatial variability in the performance of the wind turbines over
relatively short distances ($\sim 1\text{--}5$ km), unrelated to wakes, and over simple terrain.

3.3 Instantaneous wind speed and wakes

282 This section assesses snapshots of the flow field to describe spatial variations in the mean flow and turbulence structures.
Figure 6 shows the instantaneous wind speed maps at a fixed height of 90 m AGL at 05:00, 05:10 and 05:20 UTC for the
284 simulation with the turbines. The flow field over these 20 minutes contains similarities (Fig. 6a–c), such as the higher wind
speed over the second and third rows and lower wind speed over the first row. Nonetheless, temporal variability in the flow field
286 also occurs. At 05:00 UTC, the front row has weaker winds in the westernmost turbines, stronger winds in the center, followed
by another streak of weaker winds in the easternmost turbines. At subsequent times, the spatial variability consists of weaker
288 winds in the westernmost turbines and stronger winds in the easternmost turbines. However, despite the temporal variability in
the flow field, the stronger winds over the second and third rows are sustained over time.

290 Considered in a vertical slice, the flow has three regions with distinct characteristics. Figure 7 shows the instantaneous
wind speed and potential temperature at 04:54 UTC (11:54 LT) in a north-south vertical cross-section that roughly follows
292 the streamwise direction, for the simulation with and without turbines. First, a LLJ core region is near 800 m above mean sea
level (AMSL) with very strong winds and weaker turbulence (Fig. 7a–b). At the bottom of the profile, a region with high shear
294 and vigorous turbulence exists between the ground level up to about 600 m AMSL. Finally, a layer with coherent turbulence
structures induced by wind shear at the interface between both, which resemble Kelvin-Helmholtz Instabilities (KHIs), as in
296 Blumen et al. (2001); Zhou and Chow (2014) among others. The onset of KHI occurs after the second row, but has a more

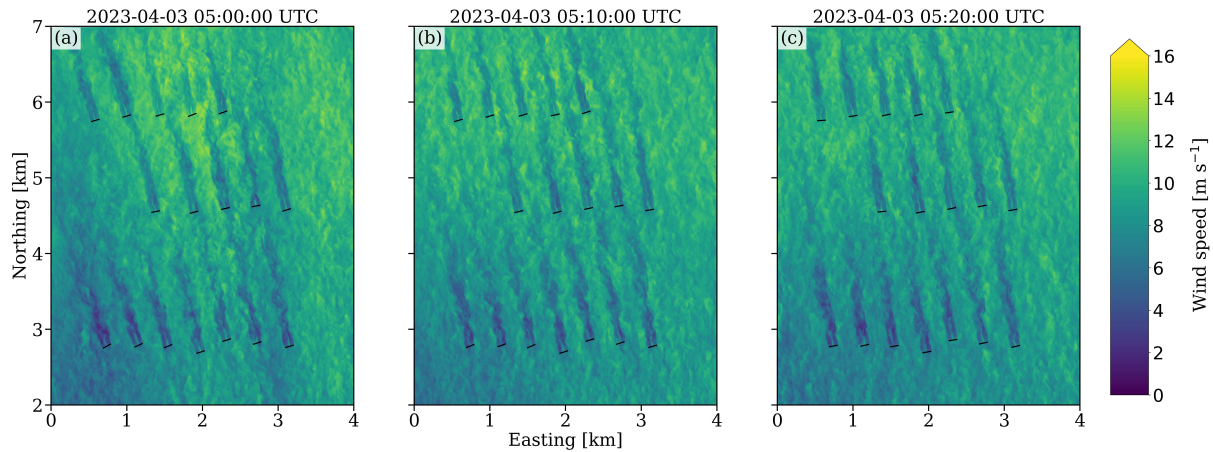


Figure 6. Instantaneous wind speed at 90 m AGL for domain D3 with the turbines at 05:00 (a), 05:10 (b) and 05:20 UTC (c) reveal that temporal fluctuations in the flow field co-exist with a sustained pattern of weaker (stronger) winds upwind (downwind). A video with the complete time window is provided as supplementary material (Radünz, 2024b).

salient structure near the third row (Fig. 7c–d). The vertical entrainment is most visible near the third row and below the LLJ
nose by assessing the potential temperature (Fig. 7c,d). The KHIs are not caused by the turbines because they also occur in
the simulation without turbines (Fig. 7b,d). However, qualitatively, the amplitude of the KHI appears to be amplified by the
presence of the turbines (Fig. 7c).

The vertical slices of wind speed and potential temperature reveal that the LLJ core region is displaced vertically (Fig. 7a–
d). Near the third row, the distance between the LLJ core region and the turbine rotor is smaller than near the first row. This
increase in wind speed associated with the downward displacement of the LLJ agrees with the spatial variability in wind speed
observed in the maps at a fixed height AGL (Fig. 6a–c).

3.4 Spatial variability in the mean wind speed and wakes

This section evaluates how the variability in the wind speed and wakes are sustained over time. Thus, the focus is the behavior
of the mean flow. First, we examine the horizontal variability in mean wind speed across different domains for the simulation
without turbines. The wider-scale domain D1 shows considerable spatial variability in wind speeds at 90 m AGL (Fig. 8a).
Domain D2 exhibits more detailed flow patterns (Fig. 8b), which includes an area with strong acceleration to the south of
domain D3 (Northing at about –10 km), followed by deceleration over the southern edge of the domain D3 (Northing at
about 0 km) and acceleration over the northern edge of the domain D3 (Northing at about 7 km). This pattern of acceleration-
deceleration-acceleration manifests across the whole of domains D1 and D2 due to terrain effects. At the highest resolution in
domain D3 and without turbines (Fig. 8c), the streamwise spatial variability in wind speed is between 6 m s^{-1} in the southwest
and 12 m s^{-1} in the north areas. In these stable conditions, the maximum wind speed does not always occur above the highest
elevation, but at a location slightly downwind of that elevation peak. Here, the strongest winds of about 12 m s^{-1} occurred

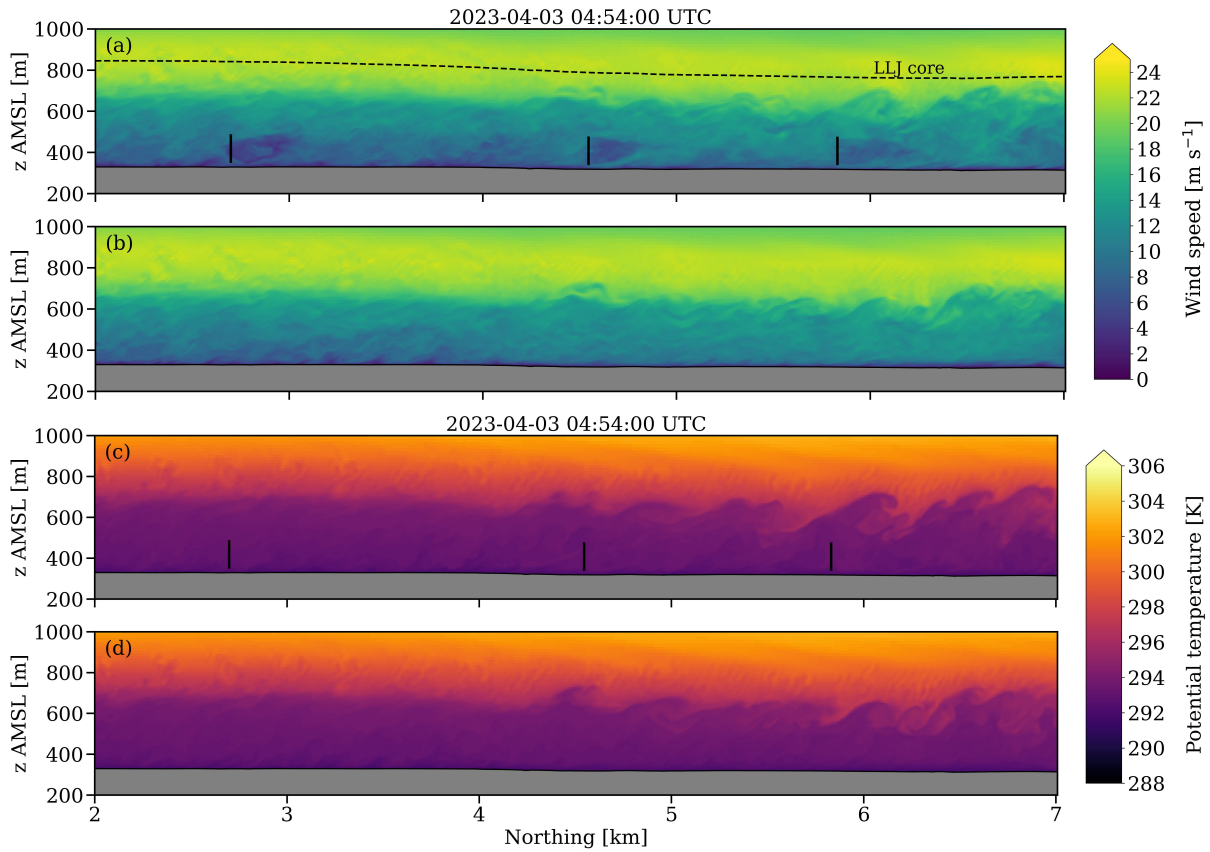


Figure 7. Vertical cross-sections in the south-north direction of wind speed (a, b) and potential temperature (c, d) for the simulation with (a, c) and without turbines (b, d). Videos with the complete time series of wind speed (Radünz, 2024d) and potential temperature (Radünz, 2024c) are provided as supplementary material.

316 over the eastern turbines of the third row (F03–F05), which are located at lower ground ($z \sim 320$ m AMSL) relative to the H05
318 turbine in the front row ($z \sim 330$ m AMSL), as shown in Fig. A1c. Notice that the turbine F01 from the third row is located
320 at the highest elevation within domain D3 (Fig. 2c), but the winds over the third row are stronger near the turbines sited over
322 lower ground (F03–F05). Thus, the relatively poor performance of the first row relative to the second and third rows is not
324 driven by the upwind blockage effect (although this is certainly present), but by the terrain-induced spatial variability in wind
326 speed.

322 Having demonstrated the influence of the terrain-induced spatial variability of winds on farm performance, we assess the
324 variability in the wake effects. To delimit the extent of the wake, the time-averaged hub-height wind speed at a fixed height of
326 90 m AGL from the simulation without turbines (Fig. 9b) was subtracted from that of the simulation with turbines (Fig. 9a)
and the wind speed deficits ($WS_{wt} - WS_{nowt}$) with magnitudes smaller than 1 m s^{-1} were filtered out (Fig. 9c). The 1 m s^{-1}
threshold is adopted because a lower threshold (0.5 m s^{-1}) causes the wakes to merge, which complicates their individual

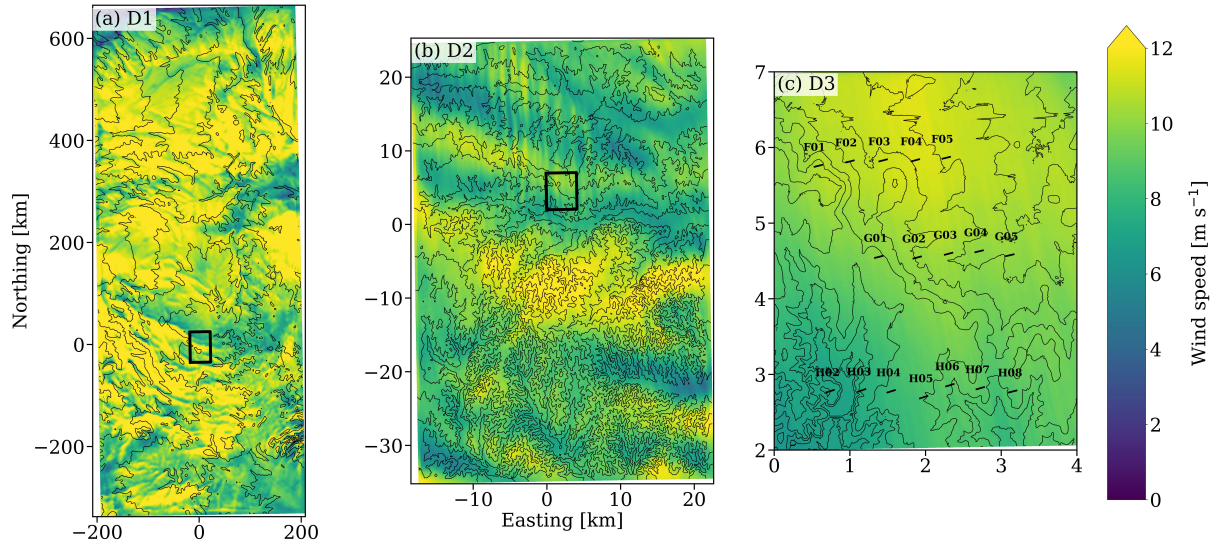


Figure 8. Time-average between 04:50 and 05:25 UTC of wind speed at 90 m AGL for domains D1 (left), D2 (center) and D3 (right) without turbines. The nested domain (black rectangle) and the vertical north-south cross-section (black line) are also illustrated.

assessment. The wakes from the first and second rows reach the downwind latitudes of the second and third rows, respectively.
328 The wake centerlines from turbines H06–H08 are not fully aligned with the rotor centerline of the downstream turbines. Thus,
the wakes only partially reach the rotors with at least a 1 m s^{-1} deficit. Conversely, the wakes from the second row flow in
330 between the turbine rotors of the third row. Interestingly, the wakes of the H02 and H03 turbines in the front row are much
shorter than the others (H04–H08) in the same row. This variability can be explained by the slower inflow wind speeds for
332 H02 and H03, which at these wind speeds, considering the thrust coefficient variability of this turbine, produce a smaller thrust
force and thus a weaker wake (Fig. C1a). Even if the thrust is lower in an absolute sense, H02–H03 are expected to have a
334 higher coefficient of thrust (C_t) compared to the other generators in the domain and based on the C_t vs WS curve (Fig. C1b).
Therefore, another possible explanation for the shorter wake of H02–H03 is the relatively stronger wake-added turbulence
336 caused by the higher C_t that can enhance wake recovery (Letizia and Iungo, 2022).

3.5 Vertical displacement and streamwise acceleration of the LLJ

338 This section analyzes how the interaction between the LLJ and the surrounding terrain leads to the observed horizontal gradients
in wind speed. The multiscale influence of the terrain on the flow field is best pictured in north-south transects of wind speed
340 (Fig. 10a–c) and vertical wind velocity (Fig. 10d–f) for domains D1, D2 and D3. The potential temperature isotherms aloft
approximate the behavior of the mean flow streamlines and reveal undulations of various scales in the flow field, most clearly
342 in domains D1 and D2. These undulations occur because, during the upslope flow, a low-level deceleration induces an upward
component to the wind speed (positive vertical wind velocity) which displaces the LLJ core upwards. Conversely, during
344 the downslope flow, a low-level acceleration occurs in phase with negative (subsiding) vertical wind velocity, and the LLJ

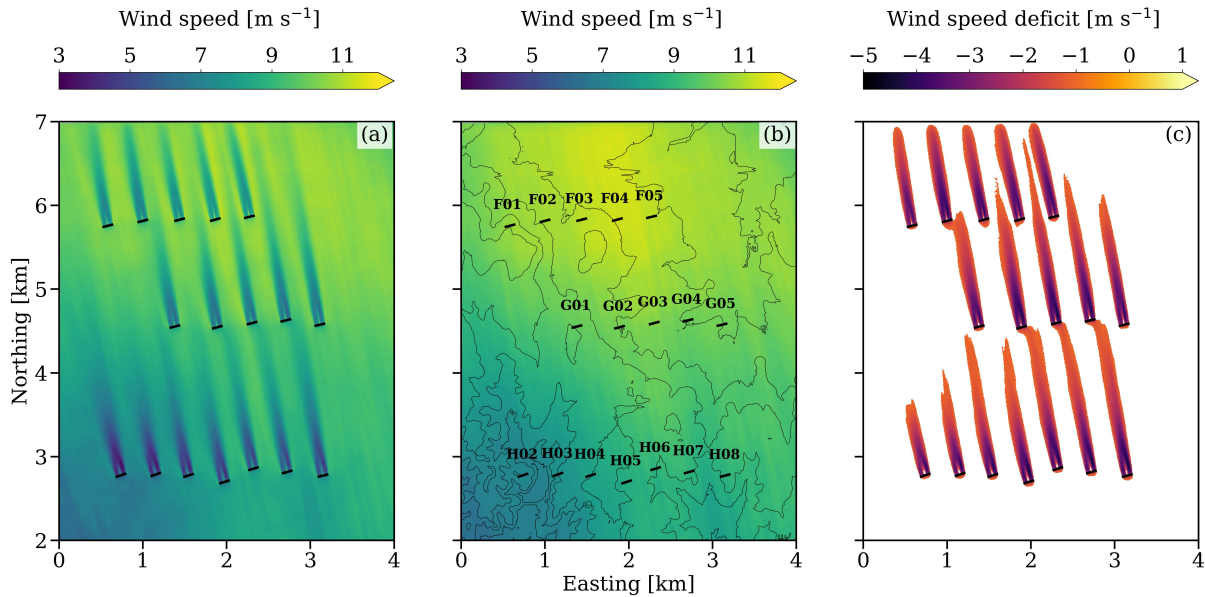


Figure 9. Time-average between 04:50 and 05:25 UTC of wind speed at hub height (90 m AGL) for the simulation with (a) and without (b) the turbines. The normalized wind speed deficit obtained by subtracting and normalizing the latter two indicates the extent of the wake region, considering a threshold of 1 m s^{-1} (c).

core is displaced downwards. The buoyancy restoring forces associated with the initial, terrain-triggered up- and downward motions create the undulations. The local maximum in wind speed occurs not at the local topographic peaks, but is shifted downwind, typical of stable boundary layers (Baines, 1995). These peaks in acceleration are visible in the D1 domain near -300 (P1), -200 (P2), -60 (P3) and -7 km (P4) (Fig. 10a), the latter being closest to King Plains. In domain D2 (Fig. 10b), both the upwind acceleration near -7 km (P4) and a downwind acceleration near 6 km (P5) are identified, the latter being the responsible for most of the wind speed spatial variability within the farm. Notice that the maximum wind speeds occur near the transition between subsiding and ascending flow (see points P4 and P5 in Fig. 10b and e) because the wind is accelerating during the downslope phase. Even though the flow field undulation appears small in the microscale domain D3 (Fig. 10c), it brings the LLJ core down, closer to turbines in the second and third rows, enough to generate a measurable effect on power.

To better delineate the terrain-induced accelerations, the spatial variability in the wind speed is expressed as the difference from a reference value, which is adopted as being the profile at the first row, f_r . Thus, the wind speed difference ($WS - WS_{f_r}$) is essentially zero at the first row (Fig. 11a). A closer examination of the finest domain (Fig. 11a) reveals the streamwise wind speed difference that can reach 3 m s^{-1} over a distance of about 3 km downwind, forming a red layer below 300 m AGL. Above the red layer near 500 m AGL, there is a white layer of either positive or negative but small wind speed differences. Finally, near 600 m AGL there is a blue layer where the wind speed difference changes sign. An examination of the wind speed differences at fixed heights AGL (Fig. 11b) reveals positive wind speed differences in the range between 2 and 3 m s^{-1} over the third row of turbines for heights below 300 m AGL.

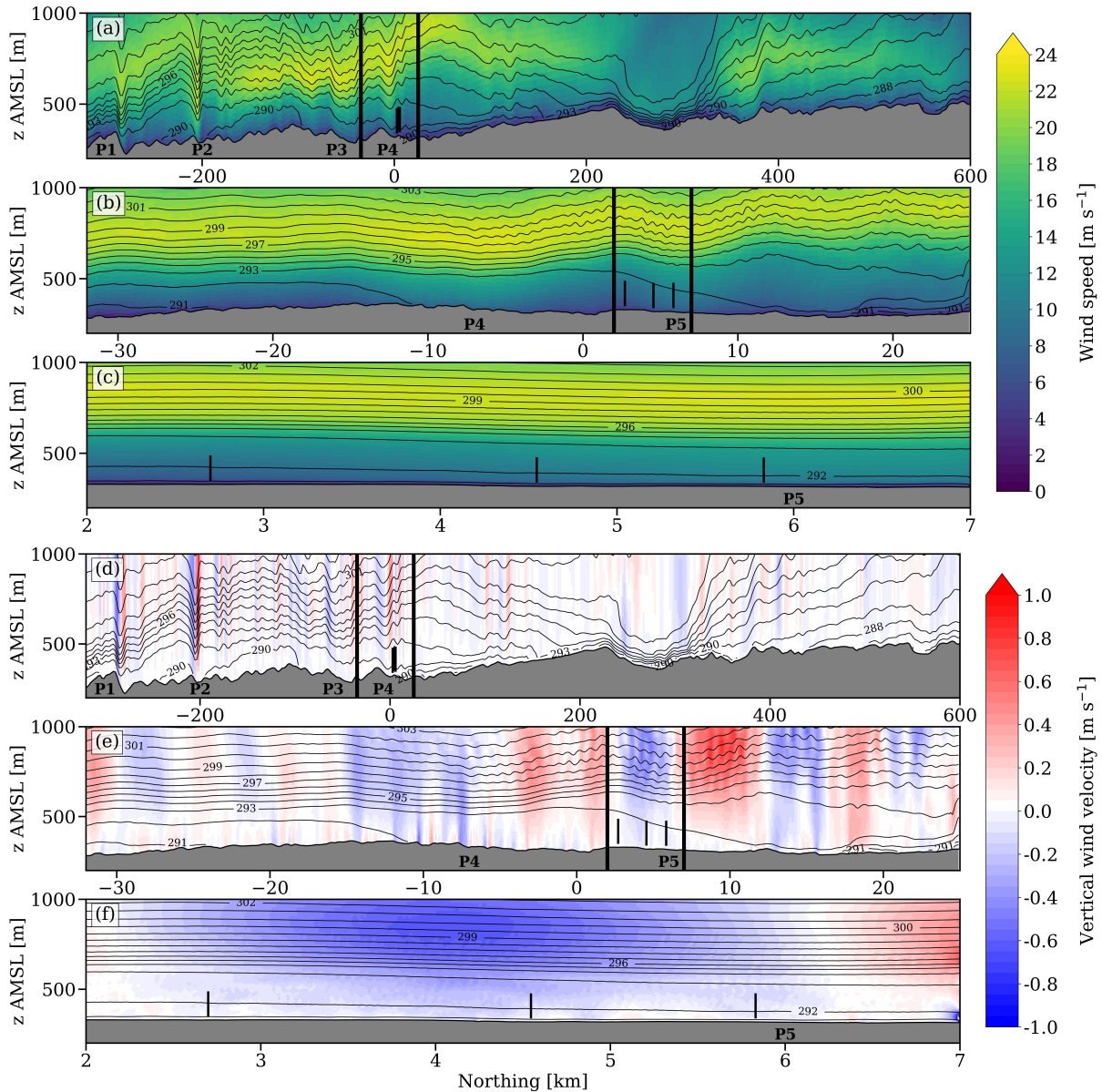


Figure 10. Vertical cross-sections in the south-north direction of wind speed (a–c) and vertical wind velocity (d–f) with potential temperature isocontours for domains D1 (a, d), D2 (b, e) and D3 (c, f). The nested domain (thick black vertical lines) and projected positions of the H05, G02 and F04 turbine rotors (thin black lines) are also shown. The points P1 to P5 mark the local maximums in wind speed induced by the terrain.

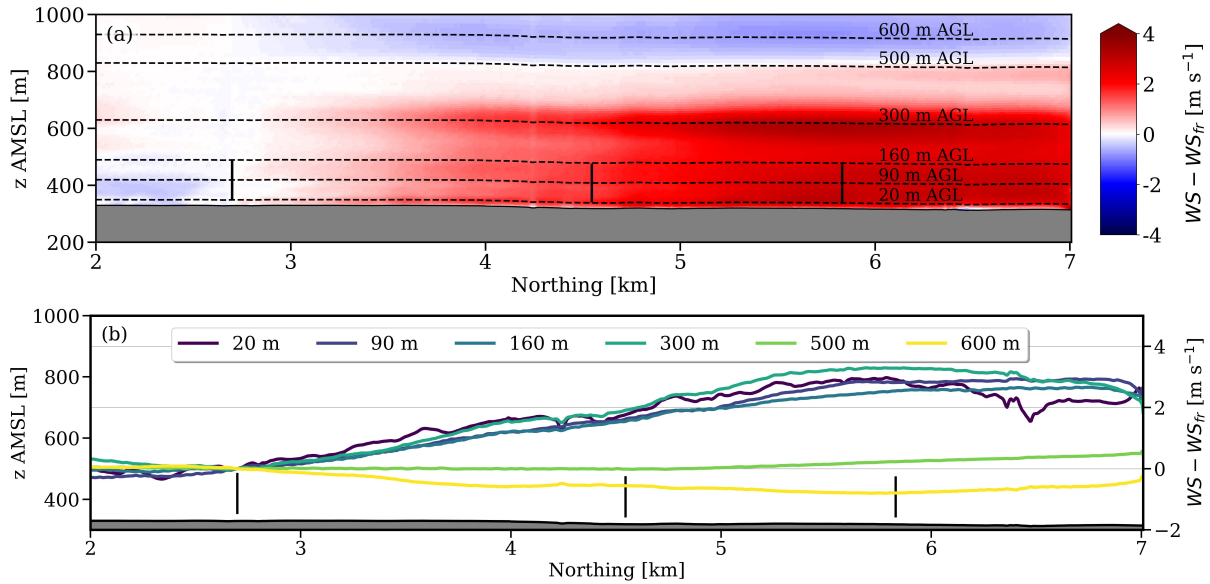


Figure 11. Vertical cross-section of wind speed difference relative to the front row profile ($WS - WS_{fr}$) for domain D3 in the simulation without turbines. The LLJ nose height is also displayed (a). Wind speed difference along terrain-following lines at fixed heights AGL (b).

362 Thus, three vertical layers with distinct wind speed difference patterns are identified above the second and third rows
 (Fig. 11a). First, the red layer with strong streamwise acceleration. Second, the white layer with near-zero streamwise ac-
 364 celeration. Third, the blue layer above the LLJ nose with small negative wind speed difference. A plausible hypothesis for
 this pattern is the combination of vertical displacement and different sign and magnitude of the wind shear. For instance, the
 366 downward displacement of the LLJ at a height AGL where the shear is large and positive (such as below the LLJ nose) will
 lead to streamwise acceleration at that height. However, the downward displacement at a height where the shear is large but
 368 negative (such as above the LLJ nose) will lead to streamwise deceleration at that height. Likewise, if the shear is very small
 (such as near the LLJ nose) the vertical displacement will produce small changes in wind speed. We will refer to this as the
 370 “rigid LLJ displacement” hypothesis. It assumes that the streamlines of the mean flow experience no change in wind speed, but
 only undulate because of the vertical displacement. Simultaneously, the actual flow acceleration along the streamlines is also
 372 quantified. This approach enables assessing the individual contributions of both effects to the overall flow field acceleration at
 several heights (Fig. 12).

374 The streamlines are computed based on the bidimensional mean wind field using as starting points the heights between 20
 and 600 m AGL near the inlet boundary (Fig. 12a). All streamlines are displaced downward (Δz) downstream of the first row
 376 (Fig. 12b). The maximum displacement occurs near the third row at a distance of 6 km and increases with height AGL. The
 displacement varies between about -15 m (20 m AGL) and -70 m (500 m AGL), and stabilizes between 500 and 600 m AGL.
 378 The actual wind speed differences along the streamlines (ΔWS_{str}) are close to 2 m s^{-1} at the lower levels (< 160 m AGL)



near the third row (Fig. 12c). At the higher levels near and above the LLJ nose (500 and 600 m AGL), the speed-up along the streamlines is weaker ($< 1 \text{ m s}^{-1}$).

The influence of the vertical displacement of the streamlines on the wind speed difference (ΔWS_{vert}) is now assessed (Fig. 12d). The vertical displacement produces small speed-ups ($\sim 1 \text{ m s}^{-1}$) below 160 m AGL near the third row; a larger speed-up ($\sim 3 \text{ m s}^{-1}$) at 300 m AGL; a small slowdown at 500 m AGL ($> -1 \text{ m s}^{-1}$); and a large slowdown at 600 m AGL ($\sim -2 \text{ m s}^{-1}$). These variations in wind speed difference across streamwise distance and height AGL are explained by the vertical variations in LLJ shear and magnitude of the downward displacement. For instance, at 300 m AGL the simulated wind shear has a local maximum (Fig. 4a) and the downward displacement is relatively large ($\Delta z \sim -50 \text{ m}$), which creates a large ΔWS_{vert} . Conversely, at 600 m AGL the simulated wind shear is negative (Fig. 4a) and the vertical displacement is even larger ($\Delta z \sim -70 \text{ m}$), which produces a large slowdown near the third row. Notice that downward displacement near the LLJ at 500 m AGL ($\Delta z \sim -70 \text{ m}$) is similar to that of 600 m AGL, but the small wind shear (Fig. 4a) leads to a small wind speed difference. Thus far, the rigid LLJ hypothesis is corroborated.

If the conceptual description makes sense, the sum of the effects from the (i) rigid LLJ displacement and (ii) the actual acceleration along the streamlines should produce speed-ups similar to those shown in Fig. 11b. Interestingly, the maximum speed-up along the streamlines ($\Delta WS_{str} \sim 2 \text{ m s}^{-1}$) occurs for the 20, 90 and 160 m AGL streamlines (Fig. 12c). The streamlines higher up at 500 and 600 m AGL attain speed-ups between 0 and 1 m s^{-1} . Thus, the terrain-induced effects are more pronounced at the lowest levels. When the vertical displacement (Fig. 12b) and the acceleration along the streamlines (Fig. 12c) are combined (Fig. 11e), they lead to a maximum speed-up of about 3 m s^{-1} for the streamlines at 20, 90 and 160 m AGL. This combined value of about 3 m s^{-1} is close to the maximum speed-up previously obtained at fixed heights AGL (Fig. 11b). The sum of ΔWS_{str} and ΔWS_{vert} also produces values consistent with Fig. 11b for the streamlines at 300, 500 and 600 m AGL.

Thus, both the (i) vertical displacement of the LLJ and the (ii) acceleration along the streamlines are important to the spatial variability in wind speed. The difference is that whereas (i) occurs at all heights and is dependent on wind shear, (ii) exerts most of its influence close to the ground. At 20 m AGL, about 18 % of the total speed-up is caused by the vertical displacement, the rest being associated with acceleration along the streamlines. This ratio increases higher up at 90 m AGL (23 %) and 160 m AGL (39 %). At 300 m AGL, the vertical displacement is responsible for most of the overall speed-up. Thus, the vertical displacement mechanism becomes more important with height because the vertical displacement also increases (Fig. 12b) and the streamlines accelerate less (Fig. 12c) with height.

4 Discussion

4.1 The role of LLJs in the terrain-induced spatial variability of nocturnal flows

In stable conditions, the low-level wind decelerates upstream of obstacles more than it would in neutral conditions because of the downward buoyancy (Mahrt and Larsen, 1990; Baines, 1995; Hunt et al., 1988) forcing the flow to stay at the same altitude rather than rising over the obstacles. Likewise, the flow accelerates more in the lee, and this combination enhances

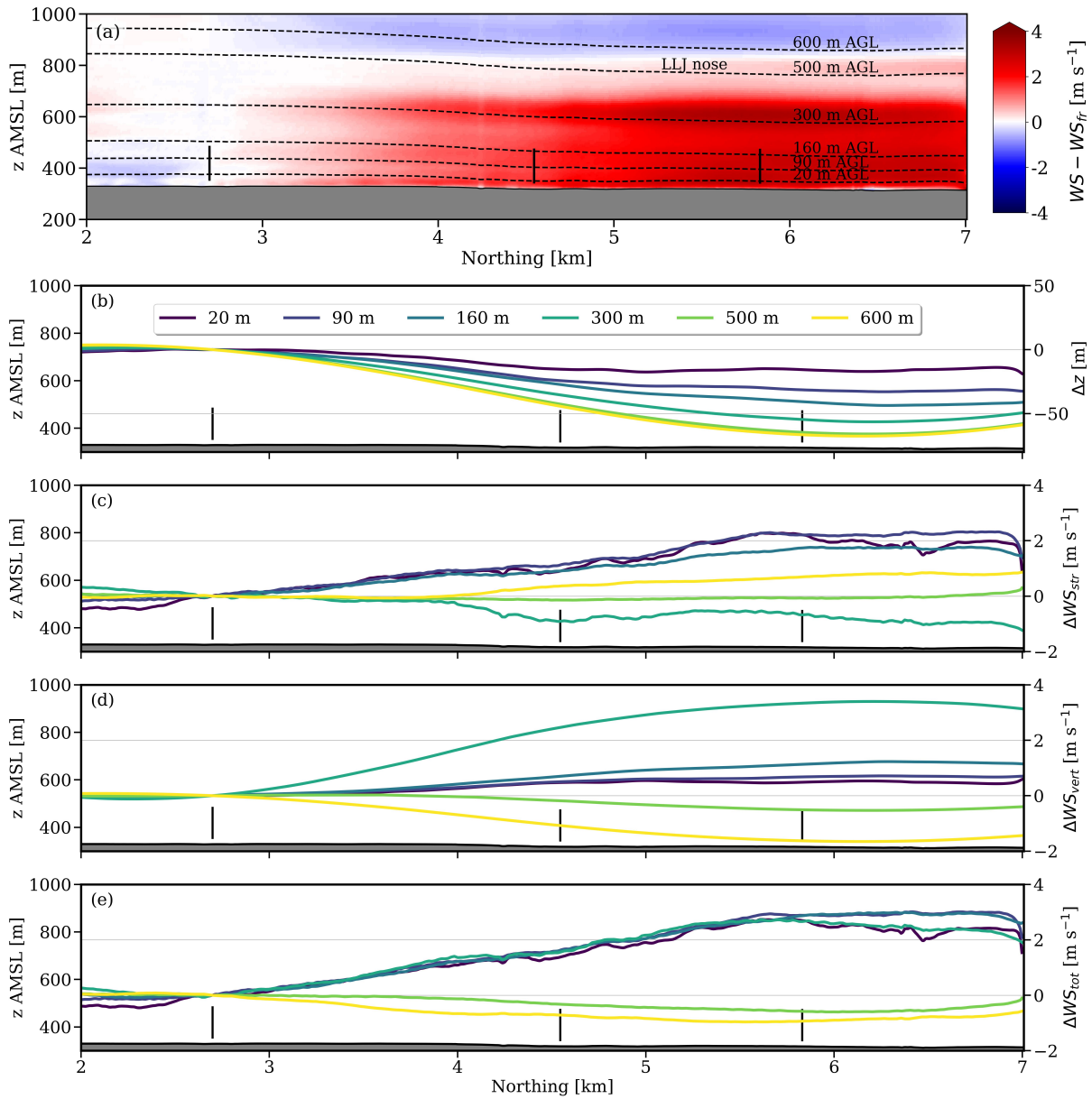


Figure 12. Vertical cross-section of wind speed difference relative to the front row profile ($WS - WS_{fr}$) for domain D3 in the simulation without turbines, with streamlines of the mean flow located between 20 and 600 m AGL near the inlet (a). The remaining subplots show the vertical displacement along the streamlines (Δz , b), actual change in wind speed along the streamlines (ΔWS_{str} , c), estimated change in wind speed caused by the vertical displacement of the LLJ (ΔWS_{vert} , d) and the estimated total change in wind speed of (c) and (d) combined (ΔWS_{tot} , e). The aforementioned variables are relative to the value at the front row.



412 the spatial variability in wind speed. The Nh/U parameter is commonly used in the literature to describe stratified flows over
topography (Baines, 1995; Sauer et al., 2016; Fernando et al., 2019). Here, $N = \sqrt{\frac{g}{T_v} \frac{\Delta\theta_v}{\Delta z}}$ is the Brunt-Vaisälä frequency, g
414 is the gravity acceleration, T_v is the virtual temperature, $\Delta\theta_v$ and Δz are the difference in potential temperature and height
between two vertical levels, respectively. Then, h is the characteristic height of the topographic feature and U is the wind
416 speed. This behavior of stratified flows over terrain occurs, to a lesser or greater extent, in any SBL, with LLJs representing a
particular case. This section explores how LLJs contribute to larger spatial variations compared to regular SBLs.

418 One key factor in this enhanced spatial variability is the high wind shear characteristic of LLJs. In Section 3.5, we identified
a mechanism whereby wind shear combined with downward displacement of the mean flow streamlines causes wind turbines
420 downstream to experience stronger winds than those upstream (Fig. 12a). Combining the magnitude of the downward displace-
ment with a reference LLJ wind speed profile at the first row, which we denoted as the “rigid LLJ hypothesis”, we demonstrated
422 that part of the spatial variability in wind speed is caused by the vertical variations in wind shear and the vertical displacement
of streamlines. For instance, below the LLJ nose where the wind shear is high and positive (Fig. 4a), the downward displace-
424 ment leads to a streamwise speed-up (the red layer in Fig. 12a, heights below 300 m AGL in Fig. 12d). Conversely, near the
LLJ nose the shear is near zero, so that the downward displacement produces very small speed-ups (the white layer in Fig. 12a,
426 at 500 m AGL in Fig. 12d).

Notice that the vertical displacement of the streamlines in the SBL is an important component for the spatial variability in
428 wind speed. In this regard, the depth of the SBL plays a key role. Idealized numerical simulations revealed that for SBLs with
the same wind speed and stratification, the case with a deeper layer produced a stronger acceleration in the lee of the obstacle
430 (Durran, 1986). Thus, the Nh/U parameter was the same, with only a difference in H_{SBL}/h , where H_{SBL} is the depth of the
SBL. One interpretation is that the buoyancy force acts over the stratified layer and it being too shallow restrains the magnitude
432 of the acceleration. This feature was discussed in experimental and theoretical works on stratified flow and obstacles (Long,
1955; Baines, 1995). More recently, a field measurement campaign and numerical simulations revealed the evolution of strong
434 downslope flow in the Alaiz mountain (Santos et al., 2020; Peña and Santos, 2021). After the evening transition, the recently
formed SBL developed into a LLJ. However, the spatial variability in the wind over the mountain becomes large only later
436 on when the SBL becomes deeper. Then, the wind accelerates down the slope and produces lee waves. A similar process was
also described in the Perdigão field campaign, where the maximum wind speed was not at the top of topographic features, but
438 rather further downstream (Fernando et al., 2019). Likewise, a wind farm with two rows of turbines located in complex terrain
experienced a similar nocturnal pattern in the wind (Radünz et al., 2021, 2022). On average, very stable conditions dominated
440 in the early nighttime, whereas weakly stable conditions dominated in the late nighttime (Radünz et al., 2021). However, the
back rows outperformed the front rows consistently only in the late nighttime. That apparent inconsistency was attributed to
442 the SBL being deeper later on, despite being less stratified (Radünz et al., 2022). One important implication of this fact is that
the LLJs later in the nighttime are likely associated with deeper SBLs and more prone to higher spatial variability. Our analysis
444 refers to 5 hours after the evening transition, which allows the SBL to develop a reasonable depth.

The relatively weak winds near the surface, caused by the high wind shear, also could make LLJs more prone to large spatial
446 variability. In Zhou and Chow (2014), multiscale LES were used to investigate cold air pooling and a turbulence intermittency



mechanism. The valley was oriented in the east-west direction (similar to ours), whereas the winds were southerly. They
448 discussed that considering the relatively simple terrain (small h) and the relatively high wind speed (high U), the low Nh/U
value suggests that the cold air would be swept away from the valley towards the north. However, the valley shelters the cold
450 air from the stronger wind aloft, so that the cold pool remains. This rationale could be adapted to interpret our results. The
strong LLJ (nose wind speed $>20 \text{ m s}^{-1}$) and the simple terrain ($h \sim 10\text{--}50 \text{ m}$) would suggest small terrain-induced effects
452 (low Nh/U). Nonetheless, because of the high shear the wind speed is considerably smaller in the rotor layer (from 6 to
10 m s^{-1}) and the Nh/U parameter is larger. Because of the higher Nh/U , the weaker surface winds are more susceptible
454 to deceleration up the slope, and consequently upper layers of the LLJ are displaced upwards. Conversely, the low-level wind
accelerates down the slope and the LLJ moves downwards. This process creates the spatial variability in wind speed (Fig. 11).
456 The flow acceleration along the streamlines, shown to be more pronounced near the ground and weaker higher up, is related to
this feature (Fig. 12b).

458 Therefore, aspects related to wind shear and SBL depth associated with the LLJ reported here, and with LLJs in general,
make it susceptible to terrain-induced accelerations. In that situation, even simple terrain can induce streamwise changes in
460 wind speed capable of significantly impacting wind farm performance patterns.

4.2 Comparison with other physical mechanisms that modulate wind farm performance in stable conditions

462 This section discusses how the terrain-induced spatial variability in wind speed compares with other physical processes that
influence farm performance in stable boundary layers, such as wind farm blockage and wakes. The literature discussion below
464 applies a spatial variability metric that measures the degree of horizontal wind speed variations associated with each process,
computed as the amplitude of the wind speed deviation or deficit caused by the process divided by a reference wind speed
466 ($\Delta WS / WS_{ref}$).

The terrain-induced variability in wind speed reported here is about 4 m s^{-1} over a distance of 5 km, or 50 % for a reference
468 wind speed of 8 m s^{-1} (Fig. 11). Consequently, the second and third downwind rows of turbines produced between 20 and
50 % more power than the first row (Fig. 5). Based on the Nh/U parameter, given the same inflow wind speed (U) and
470 stratification (N), the more complex terrain (higher h) likely amplifies the magnitude of the flow field variability relative to
simpler terrain (Baines, 1995). For instance, when Nh/U increases from 1.56 to 2.84, that produces low-level flow blockage
472 and a more acute acceleration near the lee (Fig. 5.3 in Baines (1995)). At a wind farm built over a plateau with an elevation
change of 100–150 m upwind and 160–300 m downwind, a wind speed difference of the order of $3\text{--}4 \text{ m s}^{-1}$ was identified
474 between two rows of turbines separated by a distance of about 1 km (Radünz et al., 2021, 2022). That is the same order of
variability reported here ($\sim 4 \text{ m s}^{-1}$ over 5 km) but over a much shorter distance. Not surprisingly, at times the turbines in the
476 back row in that investigation produced twice as much power as those in the front row.

In Liu and Stevens (2021), a contrasting mechanism for a terrain-induced enhancement in power performance during a LLJ
478 emerged. In the idealized LES simulation, a single wind turbine was positioned downstream of a single hill. The performance
enhancement was attributed to the higher momentum entrainment from the LLJ that was caused by the hill wake. We argue
480 that despite this mechanism being possible in other situations, during stable conditions the attached flow tends to minimize



hill wakes. Most importantly, the mechanism described by the linear wave theory and towing tank experiments (shallow water
482 equations) is unrelated to turbulent transport, but to modifications experienced by the mean flow (Baines, 1995). The terrain-
induced spatial variability in wind for stable boundary layers and LLJs literature (Santos et al., 2020; Peña and Santos, 2021;
484 Radünz et al., 2021, 2022) and the results we report on belong to the latter type (Baines, 1995).

There is consensus that wind turbine (Schepers et al., 2012; Abkar and Porté-Agel, 2015) and farm wakes (Barthelmie and
486 Jensen, 2010; Hansen et al., 2012; Abkar et al., 2016; Lundquist et al., 2018; Krishnamurthy et al., 2024; Porté-Agel et al.,
2020) recover slower in stable conditions because of the weaker entrainment of momentum into the wake. Idealized LES studies
488 report wind speed deficits between 20 and 30 % at downwind distances between $8D$ and $12D$ for a single wind turbine (Abkar
and Porté-Agel, 2015) and up to 50 % for a wind farm (Abkar et al., 2016) in stable conditions. Our results reveal a wind speed
490 deficit of about 1 m s^{-1} ($\sim 12.5 \%$) over the second and third rows of turbines (Fig. 9). In part, differences can arise from
different power curves from turbine models and operating conditions. However, high turbulence levels (Hansen et al., 2012)
492 and veer (Abkar et al., 2016) are known to enhance wake recovery. To some extent, the somewhat weaker wakes reported
here could be a byproduct of the relatively high TKE, since this LLJ is strong (Banta, 2008; Klein et al., 2015), and wind
494 veer. Therefore, the terrain-induced spatial variability in wind speed of about 4 m s^{-1} ($\sim 50 \%$) overshadows the variability
associated with the wake deficits of our study ($\sim 12.5 \%$) and scales with the deficits associated with idealized simulations of
496 wind farms in stable conditions ($< 50 \%$) (Abkar et al., 2016).

The terrain-induced spatial variability in wind influences the variability in the region of operation of individual turbine
498 power curves (Fig. C1a,b). That leads to a spatial variability in the wakes (Fig. 9c) and can have an important outcome for
wind farm control, which is considered to be most useful in the stably stratified conditions such as considered here (Fleming
500 et al., 2019). Porté-Agel et al. (2020) discussed two aspects that modulate wind farm wakes and performance. The first is the
diurnal cycle and its modulation of stability, turbulence, shear and veer, discussed in the previous paragraph. The second is
502 the presence of terrain induces a non-zero streamwise pressure gradient, vertical displacement of the wake center, and flow
separation. Based on our work, it can be added that the interplay between terrain and stability, particularly in the case of LLJs
504 (Section 4.1), is an important source of wind farm wake variability, even for simple terrain. Wind farm control, regarded as one
of the three grand challenges associated with wind energy science, is intimately linked with another grand challenge related to
506 the physics of multiscale atmosphere-wind farm interactions (Veers et al., 2019, 2022). At the core of wind farm control are
the wake effects and strategies to manipulate their intensity and propagation in the wind farm area (Meyers et al., 2022). Wind
508 farm control was shown effective in idealized numerical studies and tests in real wind farms (Fleming et al., 2019; Simley
et al., 2021). Although there were power performance benefits in neutral and convective conditions, the benefits were most
510 pronounced in stable conditions. It was pointed out that challenges in complex terrain (associated with the spatial variability of
winds) should be addressed in future studies (Meyers et al., 2022). The AWAKEN project site was selected owing to the lesser
512 terrain complexity and has ongoing wind farm control studies (Moriarty et al., 2024). The existence of spatial variability in
wake effects, as revealed by turbines H02 and H03 (Fig. 9c), highlights that accounting for terrain effects, however simple the
514 terrain may be, is important for wind farm control. However, the spatial variability in wind causes certain turbines to operate in
Region 2, whereas others operate close to or in Region 3, imparting differences in thrust force (Fig. C1a,b) and thus the wake



516 deficit. Some multiscale models, such as AMR-Wind, do not yet consider topographic effects, and how this influence will be
considered for model intercomparison and testing the AWAKEN scientific hypotheses is an open problem. Thus, wind farm
518 control strategies will likely be influenced by this terrain induced variability.

Previously, we discussed that the low-level deceleration upwind and acceleration downwind of topographic obstacles dis-
520 places the LLJ vertically, and is a source of spatial variability in wind speed (Section 4.1). A similar process occurs when wind
farm wakes decelerate the wind speed and the LLJ is displaced vertically (Wu and Porté-Agel, 2017; Larsén and Fischereit,
522 2021; Krishnamurthy et al., 2024; Quint et al., 2024) even without the presence of terrain. In a numerical investigation of a
conventionally-neutral boundary layer, the exit region of the wind farm displayed flow acceleration compared with the en-
524 trance region (Wu and Porté-Agel, 2017). Immediately downwind, the flow experienced further acceleration owing to (i) the
boundary layer adjustment and (ii) the downward displacement of the stratified free-atmosphere (their Figure 4). Even though
526 a conventionally-neutral boundary layer is different from a SBL, the concept associated with the streamwise acceleration in
the exit region and downwind is similar, the release of turbulent stresses induced by the “roughness” of the turbines. There-
528 fore, accounting for and quantifying the terrain-induced and wind-farm-induced spatial variabilities is important for wind farm
performance assessments.

530 The spatial variability associated with terrain, demonstrated here, is an order of magnitude larger than that due to upwind
blockage. According to the literature, the blockage effect may produce a maximum slowdown in the wind speed of about
532 10 % and often below 5 % (Wu and Porté-Agel, 2017; Bleeg et al., 2018; Sebastiani et al., 2021; Schneemann et al., 2021;
Sanchez Gomez et al., 2022). Using Reynolds-averaged Navier-Stokes simulations with turbines represented as actuator disks,
534 Bleeg et al. (2018) showed that the blockage effect produced an average slowdown of 3.4 % of the free wind at a distance of
two rotor diameters upwind, and an average slowdown of 1.9 % at seven to ten rotor diameters upwind. Another study used
536 multiscale simulations at the same King Plains wind farm during a LLJ episode (Sanchez Gomez et al., 2022). The slowdowns
associated with the blockage effect varied between 8 % (0.64 m s^{-1}) and 1 % immediately upwind and $24D$ upwind of the first
538 row of turbines, respectively. At an offshore wind farm during stable conditions and with turbines operating in the high-thrust
coefficient regime, the blockage was about 4 % upwind the wind farm (Schneemann et al., 2021). In Wu and Porté-Agel (2017),
540 the maximum blockage $2.5D$ upwind of the first row of turbine was 0.8 to 1.2 % (weak free-atmosphere stratification) and 10
to 11 % (strong free-atmosphere stratification). This means that the spatial variability in wind speed associated with blockage
542 ($\sim 1\text{--}10\%$) is likely one order of magnitude smaller than that of the terrain ($\sim 50\%$).

Finally, whereas the farm performance is especially sensitive to wakes and blockage in high thrust coefficient conditions and
544 environmental conditions associated with strong stratification and low TI, the terrain-induced variability can affect performance
from cut-in to near-rated wind speeds and during weaker stratification and high TI scenarios. These three effects will also
546 modulate performance differently across different wind speed, direction, stability and turbulence conditions. Also, the terrain
complexity further enhances the terrain-induced variability.



548 5 Conclusions

549 Stratified flows over terrain have always attracted scientific interest from engineers and atmospheric scientists. The flow pat-
550 terns that include lee waves and hydraulic jumps have been observed in controlled laboratory experiments as well as in field
campaigns in the natural environment. Advances in wind energy now demand a deeper understanding of the behavior of stable
552 boundary layers (SBLs) and nocturnal low-level jets (LLJs) as they interact with wind farms and the surrounding landscape.
The scientific literature generally attributes challenges to *complex terrain*, but the results we report suggest that even sites that
554 do not belong to that category, which we denote *simple terrain*, may experience important terrain-induced spatial variability in
the wind resources.

556 Using both observations and multiscale numerical simulations of a strong LLJ at the AWAKEN campaign, we show that
even simple terrain can induce important accelerations in the flow field. Furthermore, specific attributes of LLJs that may
558 separate them from regular stable boundary layers when it comes to the terrain-induced spatial variability in wind speed. For
a site in simple terrain in stable conditions, the expectation is that the downwind turbines will likely produce less energy than
560 the upwind turbines because of the wake effects. However, here, results from a realistically-forced multiscale simulation with
the WRF-LES-GAD approach were corroborated by the wind farm SCADA data to reveal that turbines in the front row were
562 actually outperformed by those in the second (SCADA = 25 %, WRF = 44 %) and third (SCADA = 51 %, WRF = 51 %) rows.
This performance variability occurred because of terrain-induced spatial variability in wind speeds, which produced stronger
564 winds over the second and third rows. The relatively simple terrain, combined with certain attributes of the LLJ, induces a
streamwise speed-up of up to 4 m s^{-1} over a distance of 5 km. The mechanism underlying this acceleration is related to the
566 vertical displacement of the LLJ combined with the high positive wind shear below its nose. Near the ground, the wind also
decelerates or accelerates along the mean flow streamlines. Higher up, the acceleration along the streamlines is smaller, and
568 the vertical displacement (undulation) of the streamlines (in response to low-level flow de/acceleration) causes the downstream
wind speeds at the same height above ground level (AGL) to increase. Conversely, near the LLJ nose where the wind shear
570 is near-zero, the vertical displacement produces small variations. Above the LLJ nose, where the wind shear is negative, the
downward displacement produces small slowdowns.

572 The terrain-induced spatial variability in wind speed associated with the LLJ has implications to the wind farm performance
and control literature. The aforementioned effect can not only be important at sites with apparently simple terrain, but also scale
574 with or even overshadow the degree of variability associated with other mechanisms that modulate wind farm performance,
such as turbine wakes and wind farm blockage. Wind farm control is regarded as one of the grand challenges in wind energy
576 science. Thus, the horizontal gradients in wind speed induced by even simple terrain should be accurately represented in the
numerical tools that implement farm control.

578 Future work should address how the long term terrain-induced spatial variability in wind speed is influenced by the diurnal
cycle. Specifically, work could assess (i) differences between the unstable (typically daytime) and stable (typically nighttime)
580 conditions, (ii) non-LLJ and LLJ stable cases and (iii) the role of the SBL depth and wind shear in the spatial variability in wind
speed. This research direction is important because more statistical significance of unstable and stable boundary layer flows



582 will enable drawing contrasts on how they modulate spatial variability in wind speed. Furthermore, it can help to elucidate
the key parameters that describe the spatial variability in wind speed. One of the main challenges is to distinguish the terrain-
584 induced acceleration effects from other processes that also produce spatial variability in wind speed, such as wind farm wakes,
blockage and dynamic events. If successful, however, this inquiry will lead to a deeper understanding of how physical processes
586 in the atmospheric boundary layer influence wind farm flows and performance in the long term. These insights can guide the
development of computational frameworks to improve the design and operation of modern wind farms.

588 *Code and data availability.* The AWAKEN observations are available online at the Data Archive Portal (DAP) at <https://a2e.energy.gov/>,
except for the turbine SCADA data, which is proprietary. Links to the observations used in this paper can be accessed at Letizia and Bodini
590 (2023); Pekour (2023); Shippert and Zhang (2016); Wharton (2023). The WRF-LES-GAD model framework version 4.3 is available at
https://github.com/a2e-mmcc/WRF/tree/mmcc_update_v4.3 (which is not the same version we used). The WRF-LES-GAD model framework
592 version 4.1.5 can be made available upon request. The terrain and land-use data can be downloaded at U.S. Geological Survey. (2020, 2019).
The HRRR data can be downloaded at National Oceanic and Atmospheric Administration (NOAA) (2024). The WRF setup files for the two
594 simulations can be accessed at Radünz (2024a).

Video supplement. Temporal evolution of streamwise transects of wind speed (Radünz, 2024d) and potential temperature (Radünz, 2024c).
596 Temporal evolution of wind speed maps at 90 m AGL (Radünz, 2024b).

Appendix A: Detailed terrain elevation profiles

598 Although the terrain might initially appear complex, the elevation variations occur over large horizontal distances. In domain
D1 (Fig. A1a), the maximum variation in elevation is approximately 300 m (\approx 500–200 m AMSL) over a horizontal distance
600 of about 900 km. In domain D2 (Fig. A1b), two notable topographic features are evident. The first is a larger feature spanning
–30 to 0 km, with a characteristic height (h) of about 60 m (\approx 360–300 m AMSL). The second is a smaller feature spanning
602 0 to 10 km, with a characteristic height of about 30 m (\approx 330–300 m AMSL).

Within the wind farm area (domain D3; Fig. A1c), elevation variations are even more subtle, with a maximum difference of
604 about 10 m (\approx 330–320 m AMSL) between the first and second/third rows of turbines. Despite this minimal elevation variation,
the downstream rows experience stronger winds (Fig. 8c) and higher energy production (Fig. 5).

606 Appendix B: Turbulence spin-up fetch

Turbulence is considered fully developed when the streamwise changes in the $\overline{w'w'}$ profile become relatively small. Near
608 the inflow boundary (Northing = 0 km), turbulence is virtually absent, as indicated by $\overline{w'w'}$ values near zero at all heights
(Fig. B1). At Northing 0.5 km, the $\overline{w'w'}$ profile exhibits overexcited turbulence compared to profiles at downstream locations

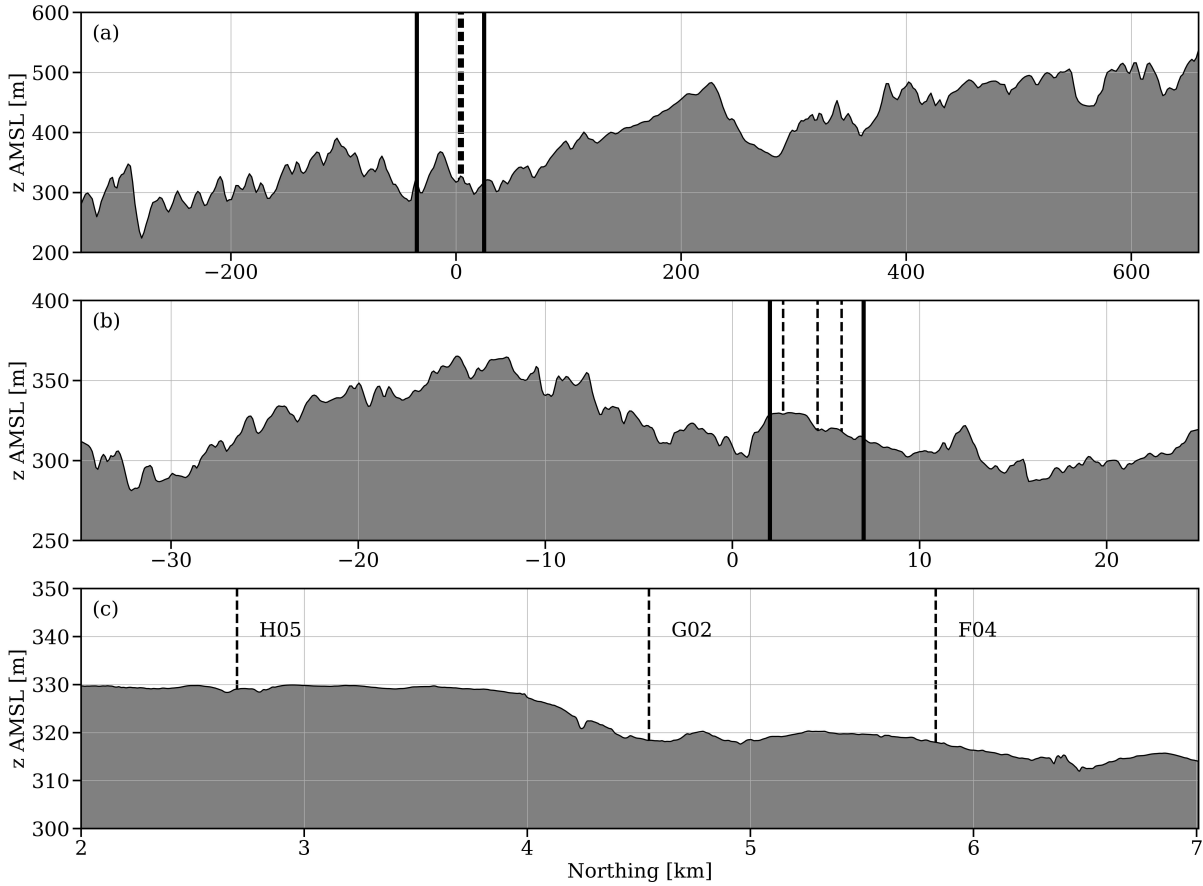


Figure A1. Terrain elevation profiles along a north-south transect for domains D1 (a), D2 (b), and D3 (c). The solid black vertical lines delimit the nested domains, while the dashed vertical lines mark the locations of turbines in the first (H05), second (G02), and third (F04) rows.

610 below 100 m AGL. Between Northing 1.5 km and 2 km, the $\overline{w'w'}$ profiles show better agreement, suggesting that turbulence
611 has spun up. The $\overline{w'w'}$ profiles in this region also align closely with those observed at the A1 site, including observational data
612 (Fig. 4e). Consequently, we adopted a 2 km fetch as the spin-up region (Fig. 2c).

Appendix C: Turbine power curves and mean wind speed

614 The spatial variability in turbine performance is evident in Fig. C1a,b. The wind speed across turbines varies significantly,
615 ranging from approximately 7 to 11 m s⁻¹, representing a difference of about 4 m s⁻¹. As a result, some turbines in the first
616 row (H02–H04) operate in Region 2 of the power curve, with generator power values between 1000 and 1500 kW (Fig. C1a).
In contrast, turbines in the third row (F01–F05) operate near or at rated capacity (2820 kW).

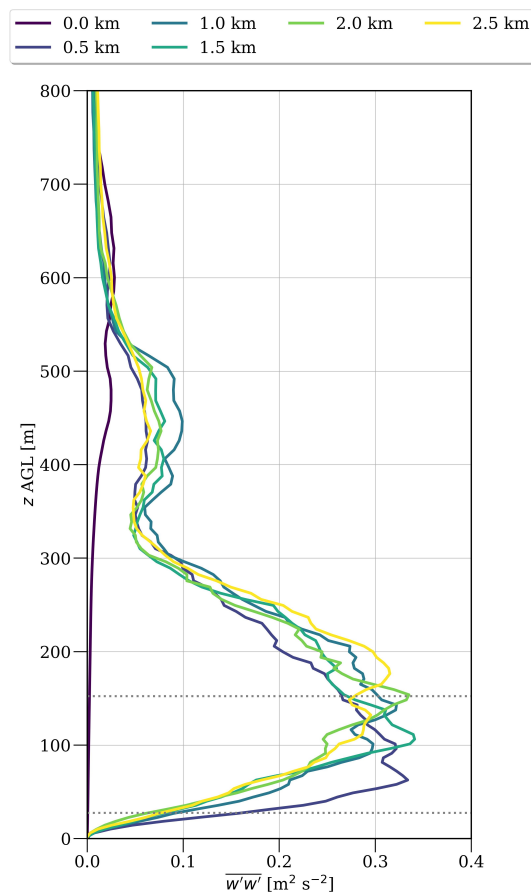


Figure B1. Profiles of vertical wind velocity variance ($\overline{w'w'}$) along a north-south transect at selected distances from the southern boundary inflow. The time average spans the period from 04:50 to 05:25 UTC, with a temporal resolution of 5 s.

618 Variability is also observed in the thrust force (Fig. C1a) and thrust coefficient (C_t) (Fig. C1b). These differences, combined
with variations in the mean wind speed that transports wakes downstream, result in complex wind speed and wake fields. This
620 complexity poses challenges for effective wind farm control.

Author contributions. WR, BSC, JKL and NH conceptualized the work. WR carried out the simulations. WR, SL and AA did the data
622 curation and formal analysis. WR did the investigation. WR, ASW, MSG and RKR worked on the simulation methodology. WR prepared
the original draft. All authors reviewed and edited the manuscript.

624 *Competing interests.* At least one of the (co-)authors is a member of the editorial board of *Wind Energy Science*.

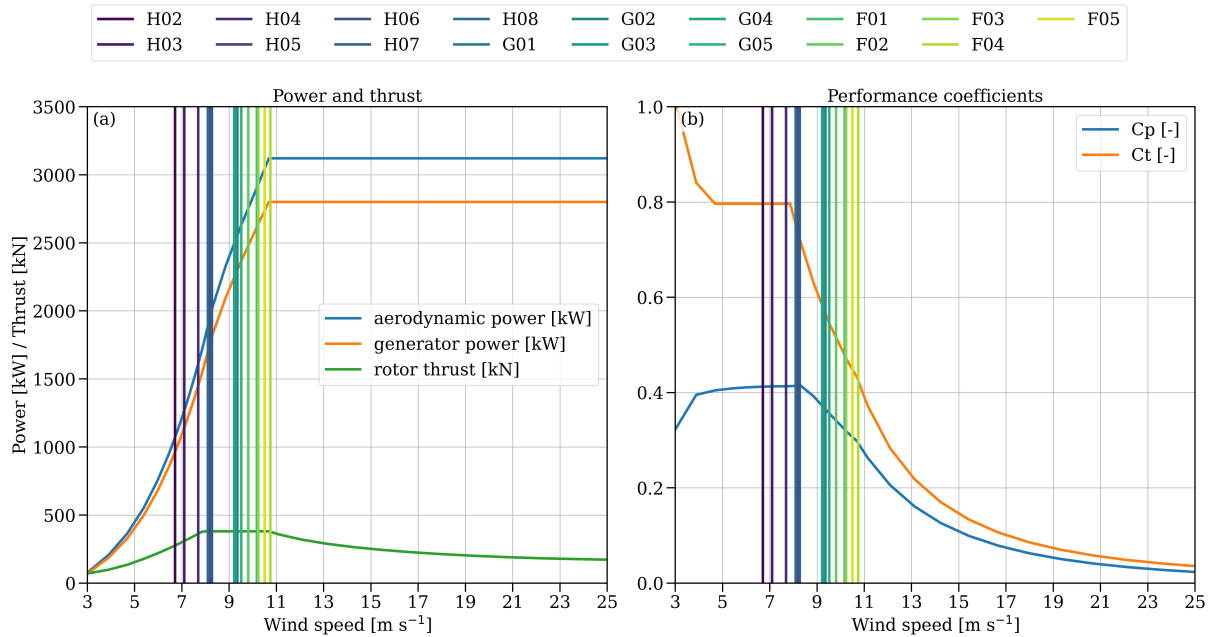


Figure C1. Aerodynamic, generator power, and rotor thrust curves for the NREL 2.82 MW turbine (Quon, 2022) used in the simulations (a). The power (C_p) and thrust (C_t) coefficient curves (b). The mean wind speed at hub height upstream of the turbines is calculated for the simulation with turbines and is shown as vertical lines.

Acknowledgements. W. Radünz would like to acknowledge the São Paulo Research Foundation (FAPESP), grant numbers 2022/04474-6 and 2023/12599-6, for financial support, and the National Renewable Energy Laboratory (NREL), operated by Alliance for Sustainable Energy, LLC, for the U.S. Department of Energy (DOE) under Contract No. DE-AC36-08GO28308, for the Eagle supercomputer resources necessary for the WRF simulations. Also, to Julie K. Lundquist for hosting him at the University of Colorado Boulder under the FAPESP grant 2023/12599-6. B. S. Carmo gratefully acknowledges partial support of the Coordenação de Aperfeiçoamento de Pessoal de Nível Superior - Brazil (CAPES) - Finance Code 001, as well as support of the RCGI – Research Centre for Gas Innovation, hosted by the University of São Paulo (USP) and sponsored by FAPESP – São Paulo Research Foundation (2020/15230-5) and TotalEnergies, and the strategic importance of the support given by ANP (Brazil’s National Oil, Natural Gas and Biofuels Agency) through the R&D levy regulation. B. S. Carmo thanks the Brazilian National Council for Scientific and Technological Development (CNPq) for financial support in the form of a productivity grant, number 314221/2021-2. P. Peixoto acknowledges support from the São Paulo Research Foundation (FAPESP), Grant 2021/06176-0, and the Brazilian National Council for Scientific and Technological Development (CNPq), Grant 303436/2022-0. ASW’s contributions were prepared by Lawrence Livermore National Laboratory under Contract DE-AC52-07NA27344, with support from the U.S. DOE Office of Energy Efficiency and Renewable Energy Wind Energy Technologies Office.



638 References

- Abkar, M. and Porté-Agel, F.: Influence of atmospheric stability on wind-turbine wakes: A large-eddy simulation study, *Physics of Fluids*,
640 27, <https://doi.org/10.1063/1.4913695>, 2015.
- Abkar, M., Sharifi, A., and Porté-Agel, F.: Wake flow in a wind farm during a diurnal cycle, *Journal of Turbulence*, 17, 420–441,
642 <https://doi.org/10.1080/14685248.2015.1127379>, 2016.
- Aitken, M. L., Kosović, B., Mirocha, J. D., and Lundquist, J. K.: Large eddy simulation of wind turbine wake dynamics in the
644 stable boundary layer using the Weather Research and Forecasting Model, *Journal of Renewable and Sustainable Energy*, 6,
<https://doi.org/10.1063/1.4885111>, 2014.
- 646 Arthur, R. S., Mirocha, J. D., Marjanovic, N., Hirth, B. D., Schroeder, J. L., Wharton, S., and Chow, F. K.: Multi-scale simulation of wind
farm performance during a frontal passage, *Atmosphere*, 11, 1–17, <https://doi.org/10.3390/atmos11030245>, 2020.
- 648 Baines, P. G.: *Topographic effects in stratified flows*, Cambridge University Press, ISBN 9780521629232, 1995.
- Banta, R., Newsom, R. K., Lundquist, J. K., Pichugina, Y. L., Coulter, R. L., and Mahrt, L.: Nocturnal Low-Level Jet Characteristics Over
650 Kansas During Cases-99, *Boundary-Layer Meteorology*, 105, 221–252, <https://doi.org/10.1023/A:101992330866>, 2002.
- Banta, R. M.: Stable-boundary-layer regimes from the perspective of the low-level jet, *Acta Geophysica*, 56, 58–87,
652 <https://doi.org/10.2478/s11600-007-0049-8>, 2008.
- Barthelmie, R. J. and Jensen, L. E.: Evaluation of wind farm efficiency and wind turbine wakes at the Nysted offshore wind farm, *Wind*
654 *Energy*, 13, 573–586, <https://doi.org/10.1002/we.408>, 2010.
- Blackadar, A. K.: Boundary Layer Wind Maxima and Their Significance for the Growth of Nocturnal Inversions, *Bulletin of the American*
656 *Meteorological Society*, 38, 283–290, <https://doi.org/10.1175/1520-0477-38.5.283>, 1957.
- Bleeg, J., Purcell, M., Ruisi, R., and Traiger, E.: Wind Farm Blockage and the Consequences of Neglecting Its Impact on Energy Production,
658 *Energies*, 11, 1609, <https://doi.org/10.3390/en11061609>, 2018.
- Blumen, W., Banta, R., Burns, S. P., Fritts, D. C., Newsom, R., Poulos, G. S., and Sun, J.: Turbulence statistics of a Kelvin–Helmholtz billow
660 event observed in the night-time boundary layer during the Cooperative Atmosphere–Surface Exchange Study field program, *Dynamics*
of Atmospheres and Oceans, 34, 189–204, [https://doi.org/10.1016/S0377-0265\(01\)00067-7](https://doi.org/10.1016/S0377-0265(01)00067-7), 2001.
- 662 Bodini, N., Abraham, A., Doubrawa, P., Letizia, S., Thedin, R., Agarwal, N., Carmo, B., Cheung, L., Corrêa Radünz, W., Gupta, A., Gold-
berger, L., Hamilton, N., Herges, T., Hirth, B., Iungo, G. V., Jordan, A., Kaul, C., Klein, P., Krishnamurthy, R., Lundquist, J. K., Maric,
664 E., Moriarty, P., Moss, C., Newsom, R., Pichugina, Y., Puccioni, M., Quon, E., Roy, S., Rosencrans, D., Sanchez Gomez, M., Scott, R.,
Shams Solari, M., Taylor, T. J., and Wharton, S.: An international benchmark for wind plant wakes from the American WAKE Experiment
666 (AWAKEN), *Journal of Physics: Conference Series*, 2767, <https://doi.org/10.1088/1742-6596/2767/9/092034>, 2024.
- Chen, F. and Dudhia, J.: Coupling an Advanced Land Surface–Hydrology Model with the Penn State–NCAR MM5 Modeling
668 System. Part I: Model Implementation and Sensitivity, *Monthly Weather Review*, 129, 569–585, [https://doi.org/10.1175/1520-0493\(2001\)129<0569:CAALSH>2.0.CO;2](https://doi.org/10.1175/1520-0493(2001)129<0569:CAALSH>2.0.CO;2), 2001.
- 670 Cheung, L., Hsieh, A., Blaylock, M., Herges, T., DeVelder, N., Brown, K., Sakievich, P., Houck, D., Maniaci, D., Kaul, C., Rai, R., Hamilton,
N., Rybchuk, A., Scott, R., Thedin, R., Brazell, M., Churchfield, M., and Sprague, M.: Investigations of Farm-to-Farm Interactions and
672 Blockage Effects from AWAKEN Using Large-Scale Numerical Simulations, *Journal of Physics: Conference Series*, 2505, 012023,
<https://doi.org/10.1088/1742-6596/2505/1/012023>, 2023.



- 674 Daniels, M. H., Lundquist, K. A., Mirocha, J. D., Wiersema, D. J., and Chow, F. K.: A new vertical grid nesting capability in the Weather Research and Forecasting (WRF) model, *Monthly Weather Review*, 144, 3725–3747, <https://doi.org/10.1175/MWR-D-16-0049.1>, 2016.
- 676 Danielson, J. J. and Gesch, D. B.: Global Multi-resolution Terrain Elevation Data 2010 (GMTED2010), Tech. rep., U.S. Department of the Interior, U.S. Geological Survey, 2011.
- 678 Deardorff, J. W.: Stratocumulus-capped mixed layers derived from a three-dimensional model, *Boundary-Layer Meteorology*, 18, 495–527, <https://doi.org/10.1007/BF00119502>, 1980.
- 680 Debnath, M., Scholbrock, A. K., Zalkind, D., Moriarty, P., Simley, E., Hamilton, N., Ivanov, C., Arthur, R. S., Barthelmie, R., Bodini, N., Brewer, A., Goldberger, L., Herges, T., Hirth, B., Valerio Iungo, G., Jager, D., Kaul, C., Klein, P., Krishnamurthy, R., Letizia, S.,
682 Lundquist, J. K., Maniaci, D., Newsom, R., Pekour, M., Pryor, S. C., Ritsche, M. T., Roadman, J., Schroeder, J., Shaw, W. J., Van Dam, J., and Wharton, S.: Design of the American Wake Experiment (AWAKEN) field campaign, *Journal of Physics: Conference Series*, 2265, 022 058, <https://doi.org/10.1088/1742-6596/2265/2/022058>, 2022.
- 684 Doosttalab, A., Siguenza-Alvarado, D., Pulletikurthi, V., Jin, Y., Bocanegra Evans, H., Chamorro, L. P., and Castillo, L.: Interaction of low-level jets with wind turbines: On the basic mechanisms for enhanced performance, *Journal of Renewable and Sustainable Energy*, 12, <https://doi.org/10.1063/5.0017230>, 2020.
- 688 Dowell, D. C., Alexander, C. R., James, E. P., Weygandt, S. S., Benjamin, S. G., Manikin, G. S., Blake, B. T., Brown, J. M., Olson, J. B., Hu, M., Smirnova, T. G., Ladwig, T., Kenyon, J. S., Ahmadov, R., Turner, D. D., Duda, J. D., and Alcott, T. I.: The High-Resolution Rapid Refresh (HRRR): An Hourly Updating Convection-Allowing Forecast Model. Part I: Motivation and System Description, *Weather and Forecasting*, 37, 1371–1395, <https://doi.org/10.1175/WAF-D-21-0151.1>, 2022.
- 690
692 Durran, D. R.: Another Look at Downslope Windstorms. Part I: The Development of Analogues to Supercritical Flow in an Infinitely Deep, Continuously Stratified Fluid, *Journal of the Atmospheric Sciences*, 43, 2527–2543, [https://doi.org/10.1175/1520-0469\(1986\)043<2527:ALADWP>2.0.CO;2](https://doi.org/10.1175/1520-0469(1986)043<2527:ALADWP>2.0.CO;2), 1986.
- 694 Fernando, H. J. S., Mann, J., Palma, J. M. L. M., Lundquist, J. K., Barthelmie, R. J., Belo-Pereira, M., Brown, W. O. J., Chow, F. K., Gerz, T., Hocut, C. M., Klein, P. M., Leo, L. S., Matos, J. C., Oncley, S. P., Pryor, S. C., Bariteau, L., Bell, T. M., Bodini, N., Carney, M. B., Courtney, M. S., Creegan, E. D., Dimitrova, R., Gomes, S., Hagen, M., Hyde, J. O., Kigle, S., Krishnamurthy, R., Lopes, J. C., Mazzaro, L., Neher, J. M. T., Menke, R., Murphy, P., Oswald, L., Otarola-Bustos, S., Pattantyus, A. K., Rodrigues, C. V., Schady, A., Sirin, N., Spuler, S., Svensson, E., Tomaszewski, J., Turner, D. D., van Veen, L., Vasiljević, N., Vassallo, D., Voss, S., Wildmann, N., and Wang, Y.: The Perdigoão: Peering into Microscale Details of Mountain Winds, *Bulletin of the American Meteorological Society*, 100, 799–819, <https://doi.org/10.1175/BAMS-D-17-0227.1>, 2019.
- 700
702 Fleming, P., King, J., Dykes, K., Simley, E., Roadman, J., Scholbrock, A., Murphy, P., Lundquist, J. K., Moriarty, P., Fleming, K., van Dam, J., Bay, C., Mudafort, R., Lopez, H., Skopek, J., Scott, M., Ryan, B., Guernsey, C., and Brake, D.: Initial results from a field campaign of wake steering applied at a commercial wind farm – Part 1, *Wind Energy Science*, 4, 273–285, <https://doi.org/https://doi.org/10.5194/wes-4-273-2019>, publisher: Copernicus GmbH, 2019.
- 704
706 Gadde, S. N. and Stevens, R. J.: Interaction between low-level jets and wind farms in a stable atmospheric boundary layer, *Physical Review Fluids*, 6, 1–25, <https://doi.org/10.1103/PhysRevFluids.6.014603>, 2021.
- 708 Hansen, K. S., Barthelmie, R. J., Jensen, L. E., and Sommer, A.: The impact of turbulence intensity and atmospheric stability on power deficits due to wind turbine wakes at Horns Rev wind farm, *Wind Energy*, 15, 183–196, <https://doi.org/10.1002/we.512>, 2012.
- 710 Hersbach, H., Bell, B., Berrisford, P., Hirahara, S., Horányi, A., Muñoz-Sabater, J., Nicolas, J., Peubey, C., Radu, R., Schepers, D., Simmons, A., Soci, C., Abdalla, S., Abellan, X., Balsamo, G., Bechtold, P., Biavati, G., Bidlot, J., Bonavita, M., De Chiara, G., Dahlgren,



- 712 P., Dee, D., Diamantakis, M., Dragani, R., Flemming, J., Forbes, R., Fuentes, M., Geer, A., Haimberger, L., Healy, S., Hogan, R. J.,
Hólm, E., Janisková, M., Keeley, S., Laloyaux, P., Lopez, P., Lupu, C., Radnoti, G., de Rosnay, P., Rozum, I., Vamborg, F., Vil-
714 laume, S., and Thépaut, J. N.: The ERA5 global reanalysis, *Quarterly Journal of the Royal Meteorological Society*, 146, 1999–2049,
<https://doi.org/10.1002/qj.3803>, 2020.
- 716 Holton, J. R.: The diurnal boundary layer wind oscillation above sloping terrain, *Tellus*, 19, 200–205,
<https://doi.org/10.3402/tellusa.v19i2.9766>, 1967.
- 718 Holtslag, A., Svensson, G., Basu, S., Beare, B., Bosveld, F., and Cuxart, J.: Overview of the GEWEX Atmospheric Boundary Layer Study
(GABLS), in: Workshop on diurnal cycles and the stable boundary layer, 7-10 November 2011, pp. 11–23, ECMWF, Shinfield Park,
720 Reading, 2012.
- Hong, S.-Y., Dudhia, J., and Chen, S.-H.: A Revised Approach to Ice Microphysical Processes for the Bulk Parameterization of Clouds and
722 Precipitation, *Monthly Weather Review*, 132, 103–120, [https://doi.org/10.1175/1520-0493\(2004\)132<0103:ARATIM>2.0.CO;2](https://doi.org/10.1175/1520-0493(2004)132<0103:ARATIM>2.0.CO;2), 2004.
- Hunt, B. J. C. R., Richards, K. J., and Brighton, P. W. M.: Stably stratified shear flow over low hills, *Quarterly Journal of the Royal Meteo-*
724 *rological Society*, 114, 859–886, 1988.
- Janić, Z. I.: Nonsingular implementation of the Mellor-Yamada level 2.5 scheme in the NCEP Meso model, Tech. rep., National Centers for
726 Environmental Prediction (U.S.), <https://repository.library.noaa.gov/view/noaa/11409>, 2001.
- Janjić, Z. I.: The Step-Mountain Coordinate: Physical Package, *Monthly Weather Review*, 118, 1429–1443, [https://doi.org/10.1175/1520-0493\(1990\)118<1429:TSMCPP>2.0.CO;2](https://doi.org/10.1175/1520-0493(1990)118<1429:TSMCPP>2.0.CO;2), 1990.
- Kaimal, J. C. and Wyngaard, J. C.: The Kansas and Minnesota experiments, *Boundary-Layer Meteorology*, 50, 31–47,
730 <https://doi.org/10.1007/BF00120517>, 1990.
- Klein, P., Bonin, T. A., Newman, J. F., Turner, D. D., Chilson, P. B., Wainwright, C. E., Blumberg, W. G., Mishra, S., Carney, M., Jacacobsen,
732 E. P., Wharton, S., and Newsom, R. K.: LABEL: A multi-institutional, student-led, atmospheric boundary layer experiment, *Bulletin of
the American Meteorological Society*, 96, 1743–1764, <https://doi.org/10.1175/BAMS-D-13-00267.1>, 2015.
- 734 Kosović, B.: Subgrid-scale modelling for the large-eddy simulation of high-Reynolds-number boundary layers, *Journal of Fluid Mechanics*,
336, 151–182, <https://doi.org/10.1017/S0022112096004697>, 1997.
- 736 Krishnamurthy, R., Newsom, R., Chand, D., and Shaw, W.: Boundary Layer Climatology at ARM Southern Great Plains, Tech. Rep. PNNL-
30832, 1779279, <https://doi.org/10.2172/1779279>, 2021a.
- 738 Krishnamurthy, R., Newsom, R. K., Chand, D., and Shaw, W. J.: Boundary Layer Climatology at ARM Southern Great Plains, Tech. Rep.
January, Pacific Northwest National Laboratory, <https://doi.org/10.2172/1778833>, 2021b.
- 740 Krishnamurthy, R., Newsom, R. K., Kaul, C. M., Letizia, S., Pekour, M., Hamilton, N., Chand, D., Flynn, D., Bodini, N., and Moriarty, P.:
Observations of wind farm wake recovery at an operating wind farm, *Wind Energy Science*, pp. 1–37, 2024.
- 742 Larsén, X. G. and Fischereit, J.: A case study of wind farm effects using two wake parameterizations in the Weather Research and Forecasting
(WRF) model (V3.7.1) in the presence of low-level jets, *Geoscientific Model Development*, 14, 3141–3158, [https://doi.org/10.5194/gmd-](https://doi.org/10.5194/gmd-14-3141-2021)
744 [14-3141-2021](https://doi.org/10.5194/gmd-14-3141-2021), 2021.
- Letizia, S. and Bodini, N.: AWAKEN Site A1 - ARM Scanning Lidar (Halo XR) / Derived Data - Wind Statistics. (04/02/2023 – 04/04/2023),
746 <https://doi.org/10.21947/1999171>, 2023.
- Letizia, S. and Iungo, G. V.: Pseudo-2D RANS : A LiDAR-driven mid-fidelity model for simulations of wind farm flows, *Journal of Renew-*
748 *able and Sustainable Energy*, 023301, <https://doi.org/10.1063/5.0076739>, 2022.



- 750 Liu, L. and Stevens, R. J.: Effects of atmospheric stability on the performance of a wind turbine located behind a three-dimensional hill, *Renewable Energy*, 175, 926–935, <https://doi.org/10.1016/j.renene.2021.05.035>, 2021.
- Long, R. R.: Some Aspects of the Flow of Stratified Fluids, *Tellus*, 7, 341–357, <https://doi.org/10.3402/tellusa.v7i3.8900>, 1955.
- 752 Lundquist, J. K.: Wind Shear and Wind Veer Effects on Wind Turbines, in: *Handbook of Wind Energy Aerodynamics*, pp. 1–22, Springer International Publishing, Cham, https://doi.org/10.1007/978-3-030-05455-7_44-1, 2021.
- 754 Lundquist, J. K., DuVivier, K. K., Kaffine, D., and Tomaszewski, J. M.: Costs and consequences of wind turbine wake effects arising from uncoordinated wind energy development, *Nature Energy*, 4, 26–34, <https://doi.org/10.1038/s41560-018-0281-2>, 2018.
- 756 Mahrt, L. and Larsen, S.: Relation of slope winds to the ambient flow over gentle terrain, *Boundary-Layer Meteorology*, 53, 93–102, <https://doi.org/10.1007/BF00122465>, 1990.
- 758 Mahrt, L., Belušić, D., and Acevedo, O.: Small-Scale Spatial Variation of the Nocturnal Wind Field, *Boundary-Layer Meteorology*, 180, 225–245, <https://doi.org/10.1007/s10546-021-00627-z>, 2021.
- 760 Mann, J., Angelou, N., Arnqvist, J., Callies, D., Cantero, E., Arroyo, R. C., Courtney, M., Cuxart, J., Dellwik, E., Gottschall, J., Ivanell, S., Kühn, P., Lea, G., Matos, J. C., Palma, J. M. L. M., Pauscher, L., Peña, A., Rodrigo, J. S., Söderberg, S., Vasiljevic, N., and Rodrigues, C. V.: Complex terrain experiments in the New European Wind Atlas, *Philosophical Transactions of the Royal Society A: Mathematical, Physical and Engineering Sciences*, 375, 20160101, <https://doi.org/10.1098/rsta.2016.0101>, 2017.
- 762 Meyers, J., Bottasso, C., Dykes, K., Fleming, P., Gebraad, P., Giebel, G., Göçmen, T., and Van Wingerden, J. W.: Wind farm flow control: Prospects and challenges, *Wind Energy Science*, 7, 2271–2306, <https://doi.org/10.5194/wes-7-2271-2022>, 2022.
- 766 Mirocha, J. D., Kosovic, B., Aitken, M. L., and Lundquist, J. K.: Implementation of a generalized actuator disk wind turbine model into the weather research and forecasting model for large-eddy simulation applications, *Journal of Renewable and Sustainable Energy*, 6, <https://doi.org/10.1063/1.4861061>, 2014.
- 768 Mlawer, E. J., Taubman, S. J., Brown, P. D., Iacono, M. J., and Clough, S. A.: Radiative transfer for inhomogeneous atmospheres: RRTM, a validated correlated-k model for the longwave, *Journal of Geophysical Research: Atmospheres*, 102, 16 663–16 682, <https://doi.org/10.1029/97JD00237>, 1997.
- 772 Moriarty, P., Bodini, N., Brugger, P., Goldberger, L., Herges, T., Hirth, B., Iungo, G. V., Ivanov, H., Kaul, C., Klein, P., Krishnamurthy, R., Letizia, S., Lundquist, K., Morris, V. R., Newsom, R., Pekour, M., Scholbrock, A., Schroeder, J., Simley, E., Wharton, S., and Zalkind, D.: Overview of Preparation for the American Wake Experiment (AWAKEN), *Journal of Renewable and Sustainable Energy*, pp. 1–42, <https://doi.org/10.1063/5.0141683>, 2024.
- 774 Muñoz-Esparza, D. and Kosovic, B.: Generation of inflow turbulence in large-eddy simulations of nonneutral atmospheric boundary layers with the cell perturbation method, *Monthly Weather Review*, 146, 1889–1909, <https://doi.org/10.1175/MWR-D-18-0077.1>, 2018.
- 778 Muñoz-Esparza, D., Kosović, B., Mirocha, J., and van Beeck, J.: Bridging the Transition from Mesoscale to Microscale Turbulence in Numerical Weather Prediction Models, *Boundary-Layer Meteorology*, 153, 409–440, <https://doi.org/10.1007/s10546-014-9956-9>, 2014.
- 780 Muñoz-Esparza, D., Kosovic, B., van Beeck, J., and Mirocha, J.: A stochastic perturbation method to generate inflow turbulence in large-eddy simulation models: Application to neutrally stratified atmospheric boundary layers, *Physics of Fluids*, 27, <https://doi.org/10.1063/1.4913572>, 2015.
- 782 Murphy, P., Lundquist, J. K., and Fleming, P.: How wind speed shear and directional veer affect the power production of a megawatt-scale operational wind turbine, *Wind Energy Science*, 5, 1169–1190, <https://doi.org/https://doi.org/10.5194/wes-5-1169-2020>, publisher: Copernicus GmbH, 2020.



- 786 Muñoz-Esparza, D., Lundquist, J. K., Sauer, J. A., Kosović, B., and Linn, R. R.: Coupled mesoscale-LES modeling of a diurnal cycle during
the CWEX-13 field campaign: From weather to boundary-layer eddies, *Journal of Advances in Modeling Earth Systems*, 9, 1572–1594,
788 <https://doi.org/10.1002/2017MS000960>, 2017.
- National Oceanic and Atmospheric Administration (NOAA): HRRR dataset download links from NOAA/AWS. Replace [HH] with
790 the hour UTC of the analysis., [https://noaa-hrrr-bdp-pds.s3.amazonaws.com/hrrr.20230402/conus/hrrr.t\[HH\]z.wrfnatf00.grib2](https://noaa-hrrr-bdp-pds.s3.amazonaws.com/hrrr.20230402/conus/hrrr.t[HH]z.wrfnatf00.grib2), [https://noaa-hrrr-bdp-pds.s3.amazonaws.com/hrrr.20230402/conus/hrrr.t\[HH\]z.wrfprsf00.grib2](https://noaa-hrrr-bdp-pds.s3.amazonaws.com/hrrr.20230402/conus/hrrr.t[HH]z.wrfprsf00.grib2), 2024.
- 792 Pekour, M.: AWAKEN Site A2 - PNNL Surface Flux Station / Raw Data. (04/02/2023 – 04/04/2023), <https://doi.org/10.21947/1898716>,
2023.
- 794 Peña, A. and Santos, P.: Lidar Observations and Numerical Simulations of an Atmospheric Hydraulic Jump and Mountain Waves, *Journal of
Geophysical Research: Atmospheres*, 126, 1–16, <https://doi.org/10.1029/2020jd033744>, 2021.
- 796 Porté-Agel, F., Bastankhah, M., and Shamsoddin, S.: Wind-Turbine and Wind-Farm Flows: A Review, *Boundary-Layer Meteorology*, 174,
1–59, <https://doi.org/10.1007/s10546-019-00473-0>, 2020.
- 798 Poulos, G. S., Blumen, W., Fritts, D. C., Lundquist, J. K., Sun, J., Burns, S. P., Nappo, C., Banta, R., Newsom, R., Cuxart, J., Terradellas,
E., Balsley, B., and Jensen, M.: CASES-99: A Comprehensive Investigation of the Stable Nocturnal Boundary Layer, *Bulletin of the
800 American Meteorological Society*, 83, 555–581, [https://doi.org/10.1175/1520-0477\(2002\)083<0555:CACIOT>2.3.CO;2](https://doi.org/10.1175/1520-0477(2002)083<0555:CACIOT>2.3.CO;2), 2002.
- Quint, D., Lundquist, J. K., and Rosencrans, D.: Offshore wind farms modify low-level jets, *Wind Energy Science Discussions*,
802 <https://doi.org/10.5194/wes-2024-48>, 2024.
- Quon, E.: NREL 2.8MW to OpenFAST 3.1.0, <https://github.com/NREL/openfast-turbine-models/tree/master/IEA-scaled/NREL-2.8-127>,
804 2022.
- Radünz, W.: WRF-LES-GAD model framework configuration files, <https://doi.org/https://doi.org/10.5281/zenodo.14210836>, 2024a.
- 806 Radünz, W.: Multiscale large-eddy simulations of a low-level jet interacting with a wind farm and terrain (wind speed at 90 m AGL),
<https://doi.org/https://doi.org/10.5281/zenodo.14193200>, 2024b.
- 808 Radünz, W.: Multiscale large-eddy simulations of a low-level jet interacting with a wind farm and terrain (vertical slices of potential temper-
ature), <https://doi.org/https://doi.org/10.5281/zenodo.14193210>, 2024c.
- 810 Radünz, W.: Multiscale large-eddy simulations of a low-level jet interacting with a wind farm and terrain (vertical slices of wind speed),
<https://doi.org/https://doi.org/10.5281/zenodo.14193192>, 2024d.
- 812 Radünz, W. C., Sakagami, Y., Haas, R., Petry, A. P., Passos, J. C., Miqueletti, M., and Dias, E.: The variability of wind re-
sources in complex terrain and its relationship with atmospheric stability, *Energy Conversion and Management*, 222, 113 249,
814 <https://doi.org/10.1016/j.enconman.2020.113249>, 2020.
- Radünz, W. C., Sakagami, Y., Haas, R., Petry, A. P., Passos, J. C., Miqueletti, M., and Dias, E.: Influence of atmospheric stability on wind
816 farm performance in complex terrain, *Applied Energy*, 282, 116 149, <https://doi.org/10.1016/j.apenergy.2020.116149>, 2021.
- Radünz, W. C., de Almeida, E., Gutiérrez, A., Acevedo, O. C., Sakagami, Y., Petry, A. P., and Passos, J. C.: Nocturnal jets over wind farms
818 in complex terrain, *Applied Energy*, 314, 118 959, <https://doi.org/10.1016/j.apenergy.2022.118959>, 2022.
- Radünz, W., Letizia, S., Scott, R., Gomez, M. S., Wise, A., Rai, R., Hamilton, N., Peixoto, P., and Carmo, B.: WRF-LES-GAD simulation
820 of the King Plains wind farm for AWAKEN during a low-level jet episode, in: Presented at the NAWEA/Windtech conference, Denver,
CO, USA, 2023.



- 822 Rai, R. K., Berg, L. K., Kosović, B., Haupt, S. E., Mirocha, J. D., Ennis, B. L., and Draxl, C.: Evaluation of the impact of horizontal
grid spacing in terra incognita on coupled mesoscale-microscale simulations using the WRF framework, *Monthly Weather Review*, 147,
824 1007–1027, <https://doi.org/10.1175/MWR-D-18-0282.1>, 2019.
- Robertson, A. N., Shaler, K., Sethuraman, L., and Jonkman, J.: Sensitivity analysis of the effect of wind characteristics and turbine properties
826 on wind turbine loads, *Wind Energy Science*, 4, 479–513, <https://doi.org/10.5194/wes-4-479-2019>, publisher: Copernicus GmbH, 2019.
- Robey, R. and Lundquist, J. K.: Behavior and mechanisms of Doppler wind lidar error in varying stability regimes, *Atmospheric Measurement
828 Techniques*, 15, 4585–4622, <https://doi.org/10.5194/amt-15-4585-2022>, 2022.
- Rogers, E., DiMego, G., Black, T., Ek, M., Ferrier, B., Gayno, G., Janjic, Z., Lin, Y., Pyle, M., Wong, V., Wu, W.-S., and Carley, J.: THE
830 NCEP NORTH AMERICAN MESOSCALE MODELING SYSTEM: RECENT CHANGES AND FUTURE PLANS, 23rd Conference
on Weather Analysis and Forecasting/19th Conference on Numerical Weather Prediction, 2009.
- 832 Sanchez Gomez, M. and Lundquist, J. K.: The effect of wind direction shear on turbine performance in a wind farm in central Iowa, *Wind
Energy Science*, 5, 125–139, <https://doi.org/https://doi.org/10.5194/wes-5-125-2020>, publisher: Copernicus GmbH, 2020.
- 834 Sanchez Gomez, M., Lundquist, J. K., Mirocha, J. D., Arthur, R. S., Muñoz-Esparza, D., and Robey, R.: Can lidars assess wind plant blockage
in simple terrain? A WRF-LES study, *Journal of Renewable and Sustainable Energy*, 14, 063 303, <https://doi.org/10.1063/5.0103668>,
836 2022.
- Santos, P., Mann, J., Vasiljevi, N., Cantero, E., Rodrigo, J. S., Borbón, F., Martínez-villagrasa, D., Martí, B., and Cuxart, J.:
838 The Alaiz Experiment: untangling multi-scale stratified flows over complex terrain, *Wind Energy Science Discussions*, pp. 1–24,
<https://doi.org/https://doi.org/10.5194/wes-2020-89>, 2020.
- 840 Sathe, A., Mann, J., Barlas, T., Bierbooms, W., and van Bussel, G.: Influence of atmospheric stability on wind turbine loads: Atmospheric
stability and loads, *Wind Energy*, 16, 1013–1032, <https://doi.org/10.1002/we.1528>, 2013.
- 842 Sathe, A., Mann, J., Vasiljevic, N., and Lea, G.: A six-beam method to measure turbulence statistics using ground-based wind lidars, *Atmo-
spheric Measurement Techniques*, 8, 729–740, <https://doi.org/10.5194/amt-8-729-2015>, 2015.
- 844 Sauer, J. A., Muñoz-Esparza, D., Canfield, J. M., Costigan, K. R., Linn, R. R., and Kim, Y. J.: A large-eddy simulation study of atmospheric
boundary layer influence on stratified flows over terrain, *Journal of the Atmospheric Sciences*, 73, 2615–2632, [https://doi.org/10.1175/JAS-
D-15-0282.1](https://doi.org/10.1175/JAS-
846 D-15-0282.1), 2016.
- Schepers, J. G., Obdam, T. S., and Prospathopoulos, J.: Analysis of wake measurements from the ECN Wind Turbine Test Site Wieringermeer,
848 EWTW, *Wind Energy*, 15, 575–591, <https://doi.org/10.1002/we.488>, 2012.
- Schneemann, J., Theuer, F., Rott, A., Dörenkämper, M., and Kühn, M.: Offshore wind farm global blockage measured with scanning lidar,
850 *Wind Energy Science*, 6, 521–538, <https://doi.org/10.5194/wes-6-521-2021>, 2021.
- Sebastiani, A., Castellani, F., Crasto, G., and Segalini, A.: Data analysis and simulation of the Lillgrund wind farm, *Wind Energy*, 24,
852 634–648, <https://doi.org/10.1002/we.2594>, 2021.
- Shippert, T. and Zhang, D.: AERIOe Thermodynamic Profile and Cloud Retrieval (AERIOEITURN), <https://doi.org/10.5439/1483830>, 2016.
- 854 Simley, E., Fleming, P., Girard, N., Alloin, L., Godefroy, E., and Duc, T.: Results from a wake-steering experiment at a commercial wind plant:
investigating the wind speed dependence of wake-steering performance, *Wind Energy Science*, 6, 1427–1453, [https://doi.org/10.5194/wes-
6-1427-2021](https://doi.org/10.5194/wes-
856 6-1427-2021), 2021.
- Skamarock, W. C.: Evaluating mesoscale NWP models using kinetic energy spectra, *Monthly Weather Review*, 132, 3019–3032,
858 <https://doi.org/10.1175/MWR2830.1>, 2004.



- 860 Skamarock, W. C., Klemp, J. B., Dudhi, J., Gill, D. O., Barker, D. M., Duda, M. G., Huang, X.-Y., Wang, W., and Powers, J. G.: A Descrip-
tion of the Advanced Research WRF Version 4. Tech. Note NCAR TN-475+STR, Tech. rep., University Corporation for Atmospheric
Research, ISBN NCAR/TN-468+STR, ISSN 1477870X, <https://doi.org/10.5065/D6DZ069T>, 2019.
- 862 Smith, E. N., Gebauer, J. G., Klein, P. M., Fedorovich, E., and Gibbs, J. A.: The great plains low-level jet during PECAN: Observed and
simulated characteristics, *Monthly Weather Review*, 147, 1845–1869, <https://doi.org/10.1175/MWR-D-18-0293.1>, 2019a.
- 864 Smith, E. N., Gebauer, J. G., Klein, P. M., Fedorovich, E., and Gibbs, J. A.: The Great Plains Low-Level Jet during PECAN: Observed and
Simulated Characteristics, *Monthly Weather Review*, 147, 1845–1869, <https://doi.org/10.1175/MWR-D-18-0293.1>, 2019b.
- 866 Stensrud, D. J.: Importance of low-level jets to climate: A review, *Journal of Climate*, 9, 1698–1711, [https://doi.org/10.1175/1520-0442\(1996\)009<1698:IOLLJT>2.0.CO;2](https://doi.org/10.1175/1520-0442(1996)009<1698:IOLLJT>2.0.CO;2), 1996.
- 868 Storm, B. and Basu, S.: The WRF model forecast-derived low-level wind shear climatology over the United States great plains, *Energies*, 3,
258–276, <https://doi.org/10.3390/en3020258>, 2010.
- 870 Storm, B., Dudhia, J., Basu, S., Swift, A., and Giammanco, I.: Evaluation of the weather research and forecasting model on forecasting
low-level jets: Implications for wind energy, *Wind Energy*, 12, 81–90, <https://doi.org/10.1002/we.288>, 2009.
- 872 Stull, R. B.: *An Introduction to Boundary Layer Meteorology*, Kluwer Academic Publishers, The Netherlands, 1988.
- Turner, D. D. and Blumberg, W. G.: Improvements to the AERIoe Thermodynamic Profile Retrieval Algorithm, *IEEE Journal of Selected*
874 *Topics in Applied Earth Observations and Remote Sensing*, 12, 1339–1354, <https://doi.org/10.1109/JSTARS.2018.2874968>, 2019.
- Turner, D. D. and Löhnert, U.: Information Content and Uncertainties in Thermodynamic Profiles and Liquid Cloud Properties Retrieved
876 from the Ground-Based Atmospheric Emitted Radiance Interferometer (AERI), *Journal of Applied Meteorology and Climatology*, 53,
752–771, <https://doi.org/10.1175/JAMC-D-13-0126.1>, 2014.
- 878 U.S. Geological Survey.: United States Geological Survey (USGS) National Land Cover Dataset 2019 1 arc-second). File:
NLCD_landcover_2011.jpg., Tech. rep., U.S. Department of the Interior, U.S. Geological Survey, [https://www.sciencebase.gov/catalog/](https://www.sciencebase.gov/catalog/item/604a4fb1d34eb120311b0039)
880 [item/604a4fb1d34eb120311b0039](https://www.sciencebase.gov/catalog/item/604a4fb1d34eb120311b0039), 2019.
- U.S. Geological Survey.: United States Geological Survey (USGS) 1/3 arc-second Digital Elevation Model. Elevation products (3DEP): 1/3
882 arc-second DEM., Tech. rep., U.S. Department of the Interior, U.S. Geological Survey, <https://apps.nationalmap.gov/downloader/#/>, 2020.
- Vanderwende, B. J., Lundquist, J. K., Rhodes, M. E., Takle, E. S., and Irvin, S. L.: Observing and simulating the summertime low-level jet
884 in central Iowa, *Monthly Weather Review*, 143, 2319–2336, <https://doi.org/10.1175/MWR-D-14-00325.1>, 2015.
- Veers, P., Dykes, K., Lantz, E., Barth, S., Bottasso, C. L., Carlson, O., Clifton, A., Green, J., Green, P., Holttinen, H., Laird, D., Lehtomäki,
886 V., Lundquist, J. K., Manwell, J., Marquis, M., Meneveau, C., Moriarty, P., Munduate, X., Muskulus, M., Naughton, J., Pao, L., Paquette,
J., Peinke, J., Robertson, A., Sanz Rodrigo, J., Sempreviva, A. M., Smith, J. C., Tuohy, A., and Wisser, R.: Grand challenges in the science
888 of wind energy, *Science*, 366, <https://doi.org/10.1126/science.aau2027>, 2019.
- Veers, P., Dykes, K., Basu, S., Bianchini, A., Clifton, A., Green, P., Holttinen, H., Kitzing, L., Kosovic, B., Lundquist, J. K., Meyers, J.,
890 O'Malley, M., Shaw, W. J., and Straw, B.: Grand Challenges: wind energy research needs for a global energy transition, *Wind Energy*
Science, 7, 2491–2496, <https://doi.org/10.5194/wes-7-2491-2022>, 2022.
- 892 Wagner, J., Gerz, T., Wildmann, N., and Gramitzky, K.: Long-term simulation of the boundary layer flow over the double-ridge site during
the Perdigão 2017 field campaign, *Atmospheric Chemistry and Physics*, 19, 1129–1146, <https://doi.org/10.5194/acp-19-1129-2019>, 2019.
- 894 Wharton, S.: AWAKEN Site A1 - LLNL Wind Cube V2 Lidar / Raw Data. (04/01/2023 – 04/04/2023), <https://doi.org/10.21947/1972653>,
2023.



- 896 Wise, A. S., Neher, J. M., Arthur, R. S., Mirocha, J. D., Lundquist, J. K., and Chow, F. K.: Meso- to microscale modeling of atmospheric
stability effects on wind turbine wake behavior in complex terrain, *Wind Energy Science*, 7, 367–386, <https://doi.org/10.5194/wes-7-367->
898 2022, 2022.
- Wise, A. S., Arthur, R. S., Abraham, A., Wharton, S., Krishnamurthy, R., Newsome, R., Hirth, B., Schroeder, J., Moriarty, P., and Chow,
900 F. K.: Large-eddy simulation of an atmospheric bore and associated gravity wave effects on wind farm performance in the Southern Great
Plains, Submitted to *Wind Energy Science*, 2024.
- 902 Wu, K. L. and Porté-Agel, F.: Flow adjustment inside and around large finite-size wind farms, *Energies*, 10, 4–9,
<https://doi.org/10.3390/en10122164>, 2017.
- 904 Wyngaard, J. C.: Toward numerical modeling in the "Terra Incognita", *Journal of the Atmospheric Sciences*, 61, 1816–1826,
[https://doi.org/10.1175/1520-0469\(2004\)061<1816:TNMITT>2.0.CO;2](https://doi.org/10.1175/1520-0469(2004)061<1816:TNMITT>2.0.CO;2), 2004.
- 906 Zhou, B. and Chow, F. K.: Nested large-eddy simulations of the intermittently turbulent stable atmospheric boundary layer over real terrain,
Journal of the Atmospheric Sciences, 71, 1021–1039, <https://doi.org/10.1175/JAS-D-13-0168.1>, 2014.